

Adaptive Behavioral Predictive Control

State-Free Regulation Without Hankel Weights

Tam W. Nguyen

POC: T. Nguyen (nguyen.tamwilly.3e@kyoto-u.ac.jp)

The behavioral view of control, introduced by Willems and Polderman [1], frames 2 dynamical systems as sets of admissible input–output trajectories rather than hidden states, and underlies many modern predictive and data-driven methods. Over the decades, the predictive 4 control framework [2], [3], [4], and its data-enabled extensions [5], [6], [7], have achieved high performance but typically rely on batch data and iterative quadratic programs (QPs), which can 6 be demanding for systems that operate continuously, face computational limits, or must adapt to slow nonlinear drift. In such settings, the need is for controllers that use streaming data directly, 8 update plant behavior online, and compute control actions in closed form. This study pursues that goal within the indirect adaptive control tradition [8], [9], [10], seeking a closed-form formulation 10 suitable for real-time operation.

The present work builds on a long sequence of ideas linking adaptation, prediction, and 12 behavior. Dual control theory, first articulated by Feldbaum [11], recognized that identification and control are inherently connected and highlighted the need for probing actions to maintain 14 learnability, a concept later formalized as persistence of excitation [12], [13]. Retrospective cost adaptive control (RCAC) developed these insights into a practical scheme by constructing a 16 retrospective performance index from streaming input–output data and updating the controller to minimize that index [14]. RCAC implemented one of the earliest adaptive controllers designed 18 for real-time digital computation and showed that recursive least-squares (RLS) adaptation could operate effectively without batch recomputation, and it has been validated in aerospace [15] and 20 active noise control [16].

Predictive cost adaptive control (PCAC) [17] extended this principle by updating a 22 predictive autoregressive-with-exogenous-input (ARX) model online via RLS and computing the future control sequence over a finite horizon using a QP with a prediction structure 24 paralleling generalized predictive control (GPC) [18], [19], [20], [21]. While structurally similar to GPC, PCAC differs by incorporating online RLS adaptation of the prediction model, 26 supporting more flexible forgetting strategies, and allowing state-constraint handling within the predictive optimization. PCAC has demonstrated effective performance in aerospace control 28 applications [22], [23], [24], [25]. The adaptive behavioral predictive control (ABPC) continues

this progression within the RCAC/PCAC framework. While PCAC has been applied successfully to nonlinear systems [26], the present formulation generalizes it by introducing explicit nonlinear regressors through kernel-based identification and retains the prediction-control organization familiar from GPC.

During closed loop, the feature dictionary spans a trajectory subspace associated with the observed input–output data. We use the term *kernel expressiveness* to denote the coverage of that subspace under the data visited in practice; it can be gauged by the rank and conditioning of the stacked prediction operators and the associated normal matrix [27]. With measured histories and frozen LPV–ARX coefficients, the one-step predictor is exact by construction, while multi-step prediction follows from Toeplitz stacking of the one-step map over the horizon (see Lemma 1). This perspective links identification and prediction directly and provides the foundation for the closed-form control computation developed in this paper.

ABPC combines recursive identification with direct predictive control in a single online framework. At each sampling instant, a kernel-based RLS algorithm updates the coefficients of a linear-parameter-varying–autoregressive-with-exogenous-input (LPV–ARX) one-step predictor using the most recent input–output data. The updated predictor is frozen over a finite horizon to form Toeplitz operators that map future inputs and outputs. The resulting quadratic cost, defined by tracking and input-penalty terms, is symmetric positive definite and admits a closed-form minimizer obtained by Cholesky factorization of the normal matrix. This procedure eliminates iterative optimization and the need for batch Hankel matrices, yielding a numerically efficient indirect adaptive controller that operates on streaming data.

The ABPC framework is consistent with established predictive and adaptive methods. With the unitary dictionary, it reduces to the unconstrained PCAC case in closed form, while nonlinear kernel regressors generalize the model structure and expand the class of representable systems. In contrast to batch Hankel-based behavioral controllers with trajectory constraints, ABPC updates its predictive model recursively. Freezing the LPV–ARX coefficients transforms the nonlinear problem into a convex surrogate with a positive definite normal matrix, enabling efficient factorization. Effective coordination is preserved when parameter variation across the horizon is small, a condition verified numerically in this study. Accordingly, the method is optimal for the frozen surrogate at each step, providing a practical balance between adaptability and computational tractability.

The numerical studies show strong performance when the kernel dictionary aligns with the underlying plant structure, including Hammerstein and nonlinear autoregressive-with-exogenous-input (NARX) systems with noncross and cross terms, as well as polynomial, cubic, and quaternion dynamics. Numerical fragility appears when the plant exhibits sinusoidal or oscillatory

behavior that polynomial features cannot represent accurately; in such cases, the unitary
2 dictionary maintains stability by implicitly capturing the internal model structure [28]. In linear
3 regimes, radial basis function kernels occasionally outperform the unitary baseline, a trend
4 consistent across runs but left open for further analysis. These observations emphasize the
influence of kernel selection and feature conditioning on closed-loop performance.

6 The main contributions are as follows:

- 1) Introduction of a kernel-based, indirect adaptive predictive controller that operates on
8 streaming data rather than batch Hankel structures.
- 2) Integration of kernel-RLS identification of an LPV-ARX predictor with Toeplitz stacking for
10 finite-horizon propagation and a closed-form Cholesky-based control computation, removing
the need for iterative optimization.
- 3) A unifying perspective that nests PCAC as a special case, connects to GPC, and extends
12 expressiveness through nonlinear dictionaries.
- 4) A systematic numerical study covering linear, Hammerstein, and NARX systems, mapping
14 kernel choice to performance and conditioning and providing practical guidance for feature
16 selection.

Concepts such as expressiveness and coefficient drift are treated qualitatively, and no formal
18 stability or robustness proofs are provided. The analysis is numerical and reproducible, emphasizing
computational feasibility and transparency of results. The remainder of the paper details the
20 identification procedure, derives the control synthesis and closed-form solution, reports numerical
studies, and concludes with limitations and future perspectives.

Input–Output System Description

2 Consider a discrete-time, unknown, causal dynamical system governed by an input–output
relationship. Let $u_k \in \mathbb{R}^m$ and $y_k \in \mathbb{R}^p$ denote the system input and output at step k , respectively.
4 At each step k , the system has received the pair (u_k, y_k) and produces the next output y_{k+1} ,
which is assumed to also depend instantaneously on the input u_{k+1} . The internal structure, such as
6 state-space realization, order, or dynamics, is entirely unknown and unmodeled. No assumptions
are made on linearity, stability, or observability.

8 We formalize the input–output system as a time-varying causal operator [29]

$$y_{k+1} = \mathcal{P}_{k+1}(y_{-\infty:k}, u_{-\infty:k+1}), \quad (1)$$

10 where $y_{-\infty:k}$ and $u_{-\infty:k+1}$ denote the input and output histories from $-\infty$ to k and $k+1$,
respectively, and \mathcal{P}_{k+1} maps these semi-infinite input–output histories into the next output. The
operator is allowed to vary with time, and no finite-dimensional realization is assumed.

12 Control Design Paradigm

14 We aim to design an optimal recursive predictor-controller operating solely on streaming
input–output data. All computations, including parameter updates and control synthesis, are
16 performed online at each step without batch optimization, generic QP, or storage of past
trajectories. Persistence of excitation is not enforced; the recursion remains well posed through
regularization, and identification quality improves if excitation arises. A design lag $\ell \geq 1$
18 specifies the temporal window of past input–output data used in the regressor. Note that this is
an algorithmic choice, not a system assumption.

20 Proposed Approach

22 Classical identification relies on parametric input–output models such as ARX and
autoregressive moving-average with exogenous input (ARMAX) [30]. These models are RLS-
24 compatible but rigid, as the basis is fixed to delays. Nonlinear extensions, such as NARX
and nonlinear autoregressive moving-average with exogenous input (NARMAX), improve
26 expressiveness by adding nonlinear functions of past signals [31]. With fixed bases, the estimation
remains linear in parameters but can be high-dimensional and ad hoc; with parameterized
nonlinearities, it becomes nonconvex.

28 We adopt a kernelized representation that enlarges the feature space beyond pure delays
while preserving convex identification [32]. Unlike Hankel-weight methods that enforce trajectory

spans under persistence of excitation [6], we make the structure explicit via a block-structured
2 kernel regressor and update it online.

The method proceeds as follows. A kernel-based predictor is updated online using RLS on
4 past input–output windows. At each step, the parameters and current past window are mapped into
LPV–ARX coefficients, which are frozen over the prediction horizon. The frozen model yields
6 a stacked affine predictor, leading to a strictly convex quadratic cost in the input sequence. The
solution is obtained in closed form by Cholesky factorization, and the first input is applied in
8 receding-horizon fashion. No batch optimization or generic QP is used.

Future inputs enter the predictor affinely (design assumption), and the LPV coefficients
10 are held fixed over each horizon. This gives an exact one-step predictor and an approximate N -
step model; accuracy improves with modest horizons and slowly varying coefficients. RLS runs
12 online with forgetting; without sufficient excitation, parameters converge on the visited subspace.
The control problem remains well posed because the quadratic cost Hessian is positive definite
14 under standard input penalties. These trade-offs are evaluated empirically in simulation.

Kernel-RLS Identification

2 For all $k \geq 0$, define the past window

$$s_k := (y_{k-\ell:k-1}, u_{k-\ell:k}), \quad (2)$$

where $\ell \geq 1$ is the lag order. Let $r = p\ell + m(\ell + 1)$. Choose a kernel dictionary $\{\gamma_j\}_{j=1}^q$ on s_k ,

4 where $\gamma_j : \mathbb{R}^r \rightarrow \mathbb{R}$. Define

$$g_k := \begin{bmatrix} \gamma_1(s_k) & \cdots & \gamma_q(s_k) \end{bmatrix}^\top \in \mathbb{R}^q. \quad (3)$$

Kernels may be mixed by concatenation (for example, radial basis function (RBF), polynomial,

6 Koopman/DMD lifts [33]).

Define the base signal vector

$$\psi_k := \begin{bmatrix} 1 \\ \text{vec}(y_{k-1}, \dots, y_{k-\ell}) \\ \text{vec}(u_k, \dots, u_{k-\ell}) \end{bmatrix} \in \mathbb{R}^{d_0}, \quad d_0 = 1 + r. \quad (4)$$

8 Using the Kronecker product, we construct the block-structured regressor in an intercept-aware form to avoid duplicate columns when a constant kernel feature is present. Let

$$g_k = \begin{bmatrix} \gamma_1(s_k) & \bar{g}_k^\top \end{bmatrix}^\top \in \mathbb{R}^q,$$

10 where the first kernel basis $\gamma_1(s) \equiv 1$ is optional and $\bar{g}_k \in \mathbb{R}^{q-1}$ collects the non-constant kernel features. Let $\bar{\psi}_k := \psi_{k,2:d_0} \in \mathbb{R}^{d_0-1}$ denote the non-intercept coordinates of ψ_k . Define

$$z_k := \begin{bmatrix} \gamma_1(s_k) \psi_k \\ \bar{g}_k \otimes \bar{\psi}_k \end{bmatrix} \in \mathbb{R}^{qd_0-(q-1)}. \quad (5)$$

12 If no constant kernel feature is present, we use the standard construction

$$z_k = g_k \otimes \psi_k \in \mathbb{R}^{qd_0}. \quad (6)$$

This keeps the intercept block $\gamma_1 \psi_k$ exactly once and forms cross-interactions only between the 14 non-constant components $(\bar{g}_k, \bar{\psi}_k)$, eliminating duplicate columns. After freezing g_k , the model remains linear in parameters and yields the LPV-ARX propagation.

16 The block-structured estimation model is

$$\hat{y}_k = \Theta z_k, \quad (7)$$

where $\hat{y}_k \in \mathbb{R}^p$ and $\Theta \in \mathbb{R}^{p \times n_z}$ with

$$n_z = \begin{cases} qd_0, & \text{if no constant kernel feature is present,} \\ q(d_0 - 1) + 1, & \text{if } \gamma_1(s) \equiv 1 \text{ is included.} \end{cases} \quad (8)$$

Note that z_k uses only measured data to estimate y_k .

² For RLS, vectorize:

$$\phi_k := z_k^\top \otimes I_p \in \mathbb{R}^{p \times d}, \quad \theta := \text{vec}(\Theta) \in \mathbb{R}^d, \quad (9)$$

where $d = pn_z$. Substituting (9) into (7) yields

$$\hat{y}_k = \phi_k \theta, \quad (10)$$

⁴ which remains linear in parameters and is therefore suitable for standard RLS.

Parameters are updated by minimizing

$$J_k(\theta) = \sum_{i=0}^k \lambda^{k-i} (y_i - \phi_i \theta)^\top (y_i - \phi_i \theta) + \lambda^k (\theta - \theta_0)^\top P_0^{-1} (\theta - \theta_0), \quad (11)$$

⁶ where $0 < \lambda \leq 1$. The minimizer admits [34]

$$L_k = P_k / \lambda, \quad (12)$$

$$P_{k+1} = L_k - L_k \phi_k^\top (I_p + \phi_k L_k \phi_k^\top)^{-1} \phi_k L_k, \quad (13)$$

$$\theta_{k+1} = \theta_k + P_{k+1} \phi_k^\top (y_k - \phi_k \theta_k), \quad (14)$$

which is initialized with θ_0 and $P_0 \succ 0$, where $P_k \in \mathbb{R}_{>0}^{d \times d}$ and I_p is the $p \times p$ identity. The ⁸ Tikhonov term ensures $P_k \succ 0$ and numerical stability.

Note that each pair (u_k, y_k) is processed once, producing θ_{k+1} without storing trajectories.

¹⁰ Under persistence of excitation, θ_k converges to the true coefficients; otherwise the recursion remains well posed and yields a stable predictor.

¹² Furthermore, although a fixed forgetting factor λ is used in all simulations, low persistence of excitation can cause ill-conditioning in RLS. No divergence was observed over the reported ¹⁴ windows, but variable-forgetting or covariance-reset strategies are recommended in general.

Control Synthesis

2 Once the parameter update θ_{k+1} has been obtained from RLS, the model is propagated
 over a finite horizon for control synthesis. The key step is to compile the identified coefficients
 4 into an LPV–ARX form and to freeze them over the prediction horizon.

Coefficient Compilation

6 The block-structured estimation model (7) in the LPV–ARX canonical form is

$$\hat{y}_k = C_k + \sum_{i=1}^{\ell} A_{k,i} y_{k-i} + \sum_{i=0}^{\ell} B_{k,i} u_{k-i}, \quad (15)$$

8 where $C_k \in \mathbb{R}^p$, $A_{k,i} \in \mathbb{R}^{p \times p}$, and $B_{k,i} \in \mathbb{R}^{p \times m}$ are the LPV coefficients. To compute them,
 partition the parameter matrix Θ_{k+1} into blocks as

$$\Theta_{k+1} = \left[\hat{C}^{(1)} \mid \hat{A}_1^{(1)} \dots \hat{A}_1^{(q)} \mid \dots \mid \hat{B}_\ell^{(1)} \dots \hat{B}_\ell^{(q)} \right], \quad (16)$$

10 where $\hat{A}_i^{(j)} \in \mathbb{R}^{p \times p}$ ($i = 1, \dots, \ell$) and $\hat{B}_i^{(j)} \in \mathbb{R}^{p \times m}$ ($i = 0, \dots, \ell$). The constant block $\hat{C}^{(1)} \in \mathbb{R}^p$
 is included only when the kernel dictionary contains a constant feature, that is, $\gamma_1(s) \equiv 1$; otherwise it is omitted and $C_k = 0$. At step k , the LPV coefficients are

$$C_k = \begin{cases} \gamma_1(s_k) \hat{C}, & \text{if a constant feature is used,} \\ 0, & \text{otherwise,} \end{cases} \quad (17)$$

$$A_{k,i} = \sum_{j=1}^q \gamma_j(s_k) \hat{A}_i^{(j)}, \quad i = 1, \dots, \ell, \quad (18)$$

$$B_{k,i} = \sum_{j=1}^q \gamma_j(s_k) \hat{B}_i^{(j)}, \quad i = 0, \dots, \ell. \quad (19)$$

12 These coefficients depend nonlinearly on past data via $\gamma_j(s_k)$ but are constants once evaluated
 at step k .

14 LPV–ARX Prediction Model

Using the coefficients $(C_k, A_{k,i}, B_{k,i})$ computed at step k , the one-step predictor is

$$y_{1|k} = C_k + \sum_{i=1}^{\ell} A_{k,i} y_{k+1-i} + \sum_{i=1}^{\ell} B_{k,i} u_{k+1-i} + B_{k,0} u_{1|k}, \quad (20)$$

16 where $y_{1|k} \in \mathbb{R}^p$ is the one-step predicted output and $u_{1|k} \in \mathbb{R}^m$ the one-step computed control.
 For $j \geq 2$, $y_{j|k}$ is obtained recursively by substituting already predicted outputs $y_{j-i|k}$ where
 18 needed.

Lemma 1 (Stacked LPV-ARX propagation). *Fix k and a horizon $N \geq 1$. Define the stacked vectors*

$$Y := \begin{bmatrix} y_{1|k} \\ \vdots \\ y_{N|k} \end{bmatrix} \in \mathbb{R}^{pN}, \quad U := \begin{bmatrix} u_{1|k} \\ \vdots \\ u_{N|k} \end{bmatrix} \in \mathbb{R}^{mN}. \quad (21)$$

Let $S_0 := I_N$ and, for $i \geq 1$, let $S_i \in \mathbb{R}^{N \times N}$ be the i -step shift matrix, whose (j, ℓ) -th entry is

$$(S_i)_{j\ell} = \begin{cases} 1, & \text{if } j - \ell = i, \\ 0, & \text{otherwise.} \end{cases}$$

Let $F_i \in \mathbb{R}^{N \times i}$ select the first i rows, that is, $F_i = \begin{bmatrix} I_i \\ 0 \end{bmatrix}$. Define

$$T_y := \sum_{i=1}^{\ell} S_i \otimes A_{k,i}, \quad T_u := \sum_{i=0}^{\ell} S_i \otimes B_{k,i}. \quad (22)$$

Collect the known initial conditions

$$Y_{\text{init}}^{(i)} := \begin{bmatrix} y_{k+1-i} \\ \vdots \\ y_k \end{bmatrix} \in \mathbb{R}^{pi}, \quad U_{\text{init}}^{(i)} := \begin{bmatrix} u_{k+1-i} \\ \vdots \\ u_k \end{bmatrix} \in \mathbb{R}^{mi}, \quad (23)$$

and define the offset

$$\sigma_k := (\mathbf{1}_N \otimes C_k) + \sum_{i=1}^{\ell} (F_i \otimes A_{k,i}) Y_{\text{init}}^{(i)} + \sum_{i=1}^{\ell} (F_i \otimes B_{k,i}) U_{\text{init}}^{(i)} \in \mathbb{R}^{pN}, \quad (24)$$

where $\mathbf{1}_N \in \mathbb{R}^N$ is the column-vector of ones.

The derived stacked affine prediction form parallels the classical finite-horizon structure used in GPC [18]. In the above form, the stacked predictions satisfy

$$(I_{pN} - T_y)Y = \sigma_k + T_u U, \quad (25)$$

yielding

$$Y = S_k + G_k U, \quad (26)$$

where $S_k := (I_{pN} - T_y)^{-1} \sigma_k$ and $G_k := (I_{pN} - T_y)^{-1} T_u$. Note that T_y is strictly block lower triangular (nilpotent). Hence, $I_{pN} - T_y$ is unit lower triangular and invertible with $(I_{pN} - T_y)^{-1} = \sum_{r=0}^{N-1} T_y^r$.

Proof: The proof is deferred to the Appendix.

Note that, according to (20), with direct feedthrough ($B_{k,0} \neq 0$), $y_{1|k}$ depends on the decision variable $u_{1|k}$ through $B_{k,0}u_{1|k}$, while all other terms use measured data (including $u_{0|k} = u_k$). For $j \geq 2$, predicted outputs $y_{j-i|k}$ enter the recursion, so multi-step accuracy under freezing is approximate and improves with modest horizons and slowly varying coefficients. If there is no direct feedthrough ($B_{k,0} = 0$), then the $N = 1$ predictor uses only measured data and is exact.

Moreover, note that G_k is block lower-triangular Toeplitz: its diagonal block is $B_{k,0}$, and the i -th subdiagonal equals the convolution of $\{A_{k,r}\}$ with $B_{k,i}$ through $(I_{pN} - T_y)^{-1}$. Furthermore, note that the form (26) justifies the quadratic cost and Cholesky solve.

Quadratic Cost and Cholesky Solution

Define the input-increment vector $\Delta U := D U - d_k$, where

$$D = \begin{bmatrix} I_m & 0 & & & 0 \\ -I_m & I_m & 0 & & \vdots \\ 0 & -I_m & I_m & \ddots & \\ \vdots & & \ddots & \ddots & 0 \\ 0 & \cdots & 0 & -I_m & I_m \end{bmatrix} \in \mathbb{R}^{mN \times mN}$$

is the block first-difference operator and $d_k = [u_k^\top \ 0 \ \dots \ 0]^\top \in \mathbb{R}^{mN}$. This gives $\Delta U = [(u_{k|k} - u_k)^\top \ (u_{k+1|k} - u_{k|k})^\top \ \dots]^\top$. The stage cost

$$J(U) = \frac{1}{2}(S_k + G_k U - R)^\top Q_y (S_k + G_k U - R) + \frac{1}{2} \Delta U^\top R_u \Delta U, \quad (27)$$

penalizes predicted tracking error and input increments, with $Q_y \succeq 0$ and $R_u \succ 0$. Expanding yields

$$J(U) = \frac{1}{2}U^\top HU + h^\top U + J_0, \quad (28)$$

where

$$H := G_k^\top Q_y G_k + D^\top R_u D \in \mathbb{R}^{mN \times mN}, \quad (29)$$

$$h := G_k^\top Q_y (S_k - R) \in \mathbb{R}^{mN}, \quad (30)$$

$$J_0 := \frac{1}{2}(S_k - R)^\top Q_y (S_k - R) \in \mathbb{R}_{\geq 0}. \quad (31)$$

The constant term J_0 does not affect the minimizer.

Well-Posedness

If $R_u \succ 0$, then $H \succ 0$ and the minimizer is unique. Alternatively, if $R_u \succeq 0$, $Q_y \succ 0$, and G_k has full column rank, then $H \succ 0$.

Solution

2 Solve $HU^* = -h$. Since H is symmetric positive definite under the conditions above,
 first compute the Cholesky factorization $H = LL^\top$ with L lower triangular (Algorithm 1). Next,
 4 solve sequentially

$$Lz = -h, \quad L^\top U^* = z, \quad (32)$$

where $z \in \mathbb{R}^{mN}$ is the intermediate vector (Algorithm 2). Then, apply the receding-horizon
 6 control $u_{k+1} = E_1 U^*$, where $E_1 = \begin{bmatrix} I_m & 0 & \dots & 0 \end{bmatrix}$.

Algorithm 1 Cholesky factorization (unblocked, lower)

Require: $H \in \mathbb{R}^{n \times n}$ with $H \succ 0$

Ensure: $L \in \mathbb{R}^{n \times n}$ lower triangular with $H = LL^\top$

```

1: for  $i = 1$  to  $n$  do
2:    $s \leftarrow H_{ii} - \sum_{k=1}^{i-1} L_{ik}^2$ 
3:    $L_{ii} \leftarrow \sqrt{s}$ 
4:   for  $j = i + 1$  to  $n$  do
5:      $t \leftarrow H_{ji} - \sum_{k=1}^{i-1} L_{jk} L_{ik}$ 
6:      $L_{ji} \leftarrow t/L_{ii}$ 
7:   end for
8: end for
9: return  $L$   $\triangleright L_{ij} = 0$  for  $j > i$ 

```

Algorithm 2 Triangular solves for $HU = b$ with $H = LL^\top$

Require: L from Alg. 1, $b \in \mathbb{R}^n$

Ensure: $x \in \mathbb{R}^n$ such that $Hx = b$

```

1: Forward solve: compute  $z$  from  $Lz = b$ 
2: for  $i = 1$  to  $n$  do
3:    $z_i \leftarrow (b_i - \sum_{k=1}^{i-1} L_{ik} z_k) / L_{ii}$ 
4: end for
5: Backward solve: compute  $x$  from  $L^\top x = z$ 
6: for  $i = n$  down to  $1$  do
7:    $x_i \leftarrow (z_i - \sum_{k=i+1}^n L_{ki} x_k) / L_{ii}$ 
8: end for
9: return  $x$ 

```

Note that, in practical applications, input–output bounds may be present. One may incorporate such constraints approximately through penalty or projection strategies (for example, input clipping or soft penalties). A detailed treatment is beyond the scope of this work.

Furthermore, note that, for initialization, one may either apply a sufficiently rich randomized input sequence to initiate excitation, or simply record the output data with zero input until the regression window is filled and then activate the controller. In practice, both approaches provide adequate initial conditions for the online RLS update, after which the controller adapts automatically.

Numerical Studies

2 This study examines the closed-loop behavior of the *adaptive behavioral predictive control* (ABPC) algorithm on systems of increasing complexity. It emphasizes systematic numerical
4 observation over formal analysis. Each example isolates one factor (stability, dimensionality, nonlinearity, or structure) to study how identification and control interact in practice.

6 **Simulation Setup**

8 All systems are treated in discrete time. For continuous-time dynamics, a fixed discretization step T_s is introduced for numerical integration and control. At the beginning of each run, a short pseudo-random binary sequence (PRBS) of fixed amplitude is applied for T_{warm} steps to
10 fill the regression window and avoid degenerate regressors. This warm-up phase ensures minimal data sufficiency, but does not assume persistence of excitation. Afterwards, the loop is closed
12 and the ABPC controller is executed for the remainder of the simulation.

14 Identification follows the RLS recursion (12)–(14) with ridge parameter $\rho > 0$, initializing the covariance as $P_0 = \rho^{-1} I_d$. The quadratic cost uses fixed weights $Q_y \succeq 0$ and $R_u \succ 0$, and is solved at each step using Algorithms 1 and 2. No input–output inequality constraints or explicit
16 saturation handling are applied.

Kernel Dictionaries

18 The feature vector g_k employed in identification concatenates a single global intercept and optional kernel-generated blocks, forming a unified representation across all dictionary types:

$$g_k = \begin{bmatrix} \gamma^{\text{uni}}(s_k) \\ \gamma^{\text{lin}}(s_k) \\ \gamma^{\text{poly},\delta}(s_k) \\ \gamma^{\text{rbf}}(s_k) \end{bmatrix},$$

20 where $q = 1 + r + q_{\text{poly}} + q_{\text{rbf}}$. Only the first coordinate is constant and equal to 1; all remaining entries depend on the current regressor $s_k \in \mathbb{R}^r$ and capture its nonlinear transformations.

The individual feature blocks are defined as

$$\gamma^{\text{uni}}(s_k) = 1, \quad (33)$$

$$\gamma^{\text{lin}}(s_k) = s_k, \quad (34)$$

$$\gamma^{\text{poly},\delta}(s_k) = \begin{bmatrix} s_k^{\otimes 1} \\ s_k^{\otimes 2} \\ \vdots \\ s_k^{\otimes \delta} \end{bmatrix}, \quad (35)$$

$$(\gamma^{\text{rbf}}(s_k))_j = \exp\left(-\frac{\|s_k - c_j\|_2^2}{2\sigma^2}\right), \quad (36)$$

2 where $j = 1, \dots, q_{\text{rbf}}$. The notation $s_k^{\otimes d}$ denotes the column vector collecting all monomials of total degree d in the components of s_k . Formally,

$$s_k^{\otimes d} := \left[\prod_{i=1}^r s_{k,i}^{e_i^{(1)}} \quad \prod_{i=1}^r s_{k,i}^{e_i^{(2)}} \quad \dots \quad \prod_{i=1}^r s_{k,i}^{e_i^{(m_d)}} \right]^\top,$$

4 where the exponent vectors $\{e^{(\ell)}\}_{\ell=1}^{m_d} \subset \mathbb{N}_0^r$ satisfy $\sum_{i=1}^r e_i^{(\ell)} = d$ and are arranged in a fixed deterministic order (for example, graded lexicographic). For example, for $r = 3$ and $d = 2$,

$$s_k^{\otimes 2} = \left[s_{k,1}^2 \quad s_{k,1}s_{k,2} \quad s_{k,1}s_{k,3} \quad s_{k,2}^2 \quad s_{k,2}s_{k,3} \quad s_{k,3}^2 \right]^\top.$$

6 Unless stated otherwise, only independent powers of each coordinate are included (no cross terms), namely,

$$s_k^{\otimes d} = \left[s_{k,1}^d \quad s_{k,2}^d \quad \dots \quad s_{k,r}^d \right]^\top.$$

8 For the RBF block, the parameters $c_j \in \mathbb{R}^r$ denote fixed Gaussian centers and $\sigma > 0$ the width of each kernel. The centers $\{c_j\}$ are drawn once from the standard normal distribution 10 $\mathcal{N}(0, I)$ and remain fixed throughout the experiment, ensuring deterministic reproducibility.

12 In the numerical studies, each kernel type is evaluated separately to isolate its contribution to model performance. A single global intercept is included for the linear and polynomial cases, while the RBF case is used without an intercept, reflecting the fact that overlapping Gaussian 14 activations already provide a constant baseline component. The resulting configurations are

$$\text{linear: } g_k = \begin{bmatrix} 1 \\ \gamma^{\text{lin}}(s_k) \end{bmatrix}, \quad \text{polynomial: } g_k = \begin{bmatrix} 1 \\ \gamma^{\text{poly},\delta}(s_k) \end{bmatrix}, \quad \text{RBF: } g_k = \gamma^{\text{rbf}}(s_k).$$

16 This convention guarantees a single intercept across all model variants and maintains consistency between theory and its implementation.

Organization of Examples

- 2 E1: *SISO linear, stable*. Command tracking for baseline validation and kernel comparison.
- 2 E2: *SISO linear, unstable*. Stabilization and disturbance rejection with frequency analysis.
- 4 E3: *MIMO linear, unstable*. Multi-channel command tracking and identification at scale.
- 4 E4: *SISO quadratic NARX without cross terms*. Core demonstration of nonlinear capability.
- 6 E5: *SISO polynomial cross-term cubic NARX*. Extension of the quadratic NARX case to polynomial cross terms.
- 8 E6: *SISO Hammerstein benchmark*. Static nonlinearity preceding linear dynamics.
- 8 E7: *MIMO nonlinear application*. Attitude stabilization on $SO(3)$.

10 Noise is excluded from baseline figures; robustness is evaluated in the Appendix, where Examples E2 and E6 are repeated under additive measurement noise.

Example 1. SISO Linear, Stable

2 Consider the discrete-time SISO linear system

$$y_k = 1.5 y_{k-1} - 0.7 y_{k-2} + 0.5 u_k + 0.3 u_{k-1}. \quad (37)$$

Its transfer function in the z -domain is

$$G(z) = \frac{0.5 z^2 + 0.3z}{z^2 - 1.5 z + 0.7}. \quad (38)$$

4 The plant poles are $0.75 \pm 0.371j$ (modulus $0.837 < 1$); the zeros are at $z_0 = 0$ and $z_1 = -0.6$ (minimum phase). Initial conditions: $y_{-1} = y_{-2} = u_0 = u_{-1} = 0$. This example is used as a
6 baseline case to illustrate the ABPC procedure and performance under a stable and noise-free setting.

8 All runs are deterministic with random seed 42. The input–output dimensions are $p = m = 1$, regressor lag $\ell = 2$, and total simulation length $T = 250$. The first $T_{\text{warm}} = 50$ samples form
10 a warm-up period used to fill the identification window. RLS uses forgetting factor $\lambda = 1.0$ and
12 ridge regularization $\rho = 10^{-9}$; numerical jitter $\varepsilon = 10^{-12}$ is added where required for symmetry and positive definiteness.

14 The predictive horizon is $N = 16$, covering about 95 % of the dominant pole decay. No
inequality constraints or input clipping are applied. The weights are $Q_y = I_N$ and $R_u = \rho_u I_N$,
where $\rho_u = 10^{-3}$.

16 During the warm-up, the plant is shortly excited by a PRBS (dwell 5-15 steps) with
amplitude 0.10. After the warm-up, the reference r_k consists of three 50-step plateaus:

$$r_k = \begin{cases} 1.0, & k \in [51, 100], \\ -0.5, & k \in [101, 150], \\ 0.75, & k \in [151, 200], \\ 0, & \text{otherwise.} \end{cases} \quad (39)$$

18 Each kernel type is evaluated under identical conditions. The polynomial kernel uses
degree $\delta = 2$ with $q_{\text{poly}} = 4$ features, while the RBF kernel uses width $\sigma = 10^3$ with a single
20 center ($q_{\text{rbf}} = 1$), where the center $c_1 \in \mathbb{R}^r$ is drawn once from $\mathcal{N}(0, I)$ using a fixed random
seed to ensure reproducibility.

22 Performance is evaluated during control, that is, over $k \in [51, 250]$, using the root-mean-square error (RMSE) and integral absolute error (IAE):

$$\text{RMSE} = \sqrt{\frac{1}{n} \sum_k (r_k - y_k)^2}, \quad \text{IAE} = \sum_k |r_k - y_k|.$$

Input activity is characterized by the total variation $\text{TV}(u) = \sum_k |u_{k+1} - u_k|$ and the maximum amplitude $\|u\|_\infty = \max_k |u_k|$. The instantaneous prediction error magnitude $|\hat{y}_k - y_k|$ is shown in logarithmic scale to indicate the stepwise accuracy of the identified model.

The closed-loop results of Example 1 are summarized in Figures 1–3. All kernel configurations achieve stable tracking of the reference signal, with close-to-zero steady-state errors. The one-step prediction errors gradually decrease and reach a plateau after each command step, showing short transient peaks at reference changes due to renewed excitation. Among all kernels, the unitary case yields the smallest residual error, whereas the RBF kernel is least accurate during the first three steps but becomes most accurate by the fourth in the noise-free case.

The performance metrics are reported in Table 1. All kernel configurations achieve nearly identical closed-loop performance, with $\text{RMSE} \approx 0.017$, $\text{IAE} \approx 0.93$, and comparable input effort ($\text{TV}_u \approx 46.4$, $\text{Peak}_u \approx 2.6$). The polynomial kernel shows a slightly higher tracking error and input activity, while the unitary, linear, and RBF kernels produce indistinguishable results within numerical precision. Overall, the responses confirm consistent controller behavior across kernel types in this linear setting.

Example 2. SISO Linear, Unstable

2 Consider the discrete-time SISO system

$$y_k = 2.0 y_{k-1} - 1.01 y_{k-2} + 0.5 u_{k-1} - 0.65 u_{k-2}. \quad (40)$$

Its transfer function is

$$G(z) = \frac{0.5z - 0.65}{z^2 - 2.0z + 1.01}. \quad (41)$$

4 The poles $1 \pm 0.1j$ have modulus $\sqrt{1.01} \approx 1.005 > 1$, hence the plant is unstable. The zero
 at $z_0 = 1.3$ lies outside the unit circle, so the plant is nonminimum-phase. Initial conditions:
 6 $y_{-1} = y_{-2} = u_{-1} = u_{-2} = 0$. This plant tests the ability of the ABPC controller to stabilize an
 unstable, NMP process during online identification. The control task is regulation to the origin,
 8 that is, $r_k = 0$.

Next, we consider the perturbed system

$$y_k = 2.0 y_{k-1} - 1.01 y_{k-2} + 0.5 u_{k-1} - 0.65 u_{k-2} + d_k, \quad d_k = A \cos(\omega k), \quad (42)$$

10 where $A \in \mathbb{R}_{>0}$ is the amplitude, and $\omega \in [0, \pi]$ is the disturbance frequency (radians/sample).
 By sweeping ω and measuring the steady-state RMS of y_k after transient decay, an empirical
 12 closed-loop disturbance-to-output gain (sensitivity curve) is obtained for each kernel.

14 A short warm-up of $T_{\text{warm}} = 5$ samples to avoid divergence before closing the loop. The
 subsequent RMS measurements exclude this warm-up window.

Stabilization

16 This example targets closed-loop stabilization. All parameters are identical to those in
 Example 1 except for the horizon and the control weight, which are set to $N = 20$ and $\rho_u =$
 18 3.5×10^3 , respectively.

20 Figure 4 shows the closed-loop stabilization results for the stable SISO linear system
 under all kernel specifications. All responses start from a positive value and display an initial
 22 negative excursion before settling around the origin. The RBF kernel yields the fastest decay
 and smallest oscillation amplitude, followed by the unitary, linear, and polynomial kernels in
 that order. Although all responses stabilize, the polynomial kernel exhibits more pronounced
 24 oscillations and slower attenuation. The logarithmic error traces confirm the same trend, with
 the RBF kernel maintaining the lowest overall error magnitude.

26 Figure 5 displays the identified LPV-ARX coefficients over the first 60 steps, corresponding
 to the transient learning phase. For both A_k and B_k , the RBF and unitary kernels reach their

steady values within the PRBS window, while the linear and polynomial kernels require longer adaptation intervals, approximately 20 and 45 steps, respectively. All coefficients remain steady after this window, though not shown for brevity. For C_k , the RBF kernel yields a constant zero term as the intercept is already represented in its feature set, whereas the unitary, linear, and polynomial kernels approach zero at increasing rates consistent with their adaptation speeds.

Table 2 shows that all kernels achieve stabilization, with performance ordered by RBF, unitary, linear, and polynomial. The RBF kernel yields the lowest tracking error and control effort, as seen from its smallest RMSE, IAE, and TV_u values. Unitary follows closely, providing stable behavior with moderate control activity. Linear and polynomial kernels exhibit larger steady-state fluctuations and higher integrated error, with the polynomial also showing the largest control variation and peak amplitude. These quantitative results are consistent with the transient observations in Figures 4 and 5.

Disturbance Rejection

This example extends Example 2a by including a frequency-domain assessment of disturbance rejection. Figure 6 (unitary) and Figure 7 (RBF) present time responses and logarithmic instantaneous output energy at fixed $\omega = \pi/4$. In the unitary case, all runs remain bounded. Transients are largest at $\ell = 3$, while increasing the lag to $\ell \geq 4$ reduces oscillations and yields low, stable steady levels consistent with the log plots. In the RBF case, performance is more lag sensitive. The case $\ell = 2$ does not suppress the disturbance reliably and may drift as amplitude increases, $\ell = 3$ becomes unstable at moderate and large amplitudes, and $\ell \geq 4$ produces consistent suppression with steady low energy.

With an output sinusoid, the one-step prediction error becomes correlated with the regressors. Linear and polynomial dictionaries do not span sinusoidal modes. Thus, a structured residual remains outside $\text{span}\{\phi_k\}$. RLS then updates toward an unattainable fit, which manifests as “parameter chasing” and growth of P_k even with $\lambda = 1$. In this setting, we were not able to stabilize the closed loop using linear or polynomial features. Therefore, this example focuses on unitary and RBF, which achieve reliable suppression once the lag is sufficiently high.

Table 3 complements the time-domain plots and confirms the observed trends. For the unitary kernel, all runs remain bounded, though large transients arise for $\ell = 3$, where both RMSE and IAE increase by more than two orders of magnitude compared with other cases. At each amplitude, performance improves monotonically with lag order: $\ell = 2$ yields the poorest steady-state error, while $\ell = 4$ and $\ell = 5$ achieve the lowest RMSE and IAE with moderate control effort. For instance, at $A = 1$, the metrics drop from RMSE = 27.26 at $\ell = 2$ to about 1.9 at $\ell = 4$ and $\ell = 5$, accompanied by a sharp decrease in TV_u . This matches the visual

evidence of smooth, stable trajectories for higher ℓ .

For the RBF kernel, instability appears for $\ell = 3$ at moderate and large amplitudes, where the errors diverge exponentially. At $\ell = 2$, responses remain bounded but exhibit significant drift or large residual oscillations. Only for $\ell \geq 4$ does the closed loop stabilize, with small RMSE and IAE and limited control activity. The improvement between $\ell = 3$ and $\ell = 4$ is dramatic; an increase in lag order restores disturbance suppression across all amplitudes. These results confirm that both kernels benefit from longer regressors, but the RBF kernel requires higher lag depth to achieve comparable robustness to the unitary case. Overall, numerical metrics are fully consistent with the qualitative observations from the output and log-energy figures.

Next, the disturbance amplitude is fixed to $A = 0.01$ and the lag order to $\ell = 5$. To improve numerical stability, the RBF kernel width is increased to $\sigma = 10^4$. The disturbance frequency ω is swept from 0 to π in increments of 0.05. Each simulation runs for 5000 steps, and performance is evaluated over the last $20 T_\omega$ samples, where $T_\omega = \lceil 2\pi/\omega \rceil$. Thus, the evaluation window is defined as $\mathcal{W}_\omega = [5000 - \max(400, 20 T_\omega) + 1, 5000]$. For the static case $\omega = 0$, a fixed window of 1000 samples at the end of the run is used instead. For each ω , the RMSE is computed on this window as $\text{RMSE} = \sqrt{\frac{1}{T_\omega} \sum_{k \in \mathcal{W}_\omega} y_k^2}$, with $r_k = 0$, so that the RMSE directly represents the output energy around the origin.

Figure 8 shows the frequency response of the unitary and RBF kernels. With online RLS and no forgetting ($\lambda = 1.0$), the RBF kernel remarkably remained stable and matched or slightly exceeded the unitary kernel in disturbance attenuation under the tested settings (noiseless case, $A = 0.01$, $\ell = 5$, RBF width $\sigma = 10^4$). This is an observation, not a general guarantee; it holds for our horizons, windows, and seeds.

To assess robustness, Example 2b is repeated under additive measurement noise with standard deviation 10^{-2} . All other parameters remain identical to the noiseless case. This additional test, reported in the Appendix, confirms that both kernels maintain their qualitative frequency-domain behavior and preserve effective disturbance attenuation despite measurement noise.

Example 3. MIMO Linear, Unstable

2 Consider the discrete-time MIMO linear system with three outputs and two inputs

$$y_k = A_1 y_{k-1} + A_2 y_{k-2} + B_0 u_k + B_1 u_{k-1} + B_2 u_{k-2}, \quad (43)$$

where $y_k \in \mathbb{R}^3$, $u_k \in \mathbb{R}^2$, and the system matrices are

$$A_1 = \begin{bmatrix} 1.7 & 0 & 0 \\ 0 & 1.473 & 0 \\ 0 & 0 & 1.8 \end{bmatrix}, \quad A_2 = \begin{bmatrix} -0.6 & 0 & 0 \\ 0 & -0.7225 & 0 \\ 0 & 0 & -0.81 \end{bmatrix},$$

4

$$B_0 = \begin{bmatrix} 0.4 & -0.1 \\ 0.2 & 0.3 \\ -0.1 & 0.5 \end{bmatrix}, \quad B_1 = \begin{bmatrix} 0.1 & 0 \\ -0.05 & 0.2 \\ 0 & -0.1 \end{bmatrix}, \quad B_2 = \begin{bmatrix} 0 & 0.05 \\ 0 & 0 \\ 0.08 & 0 \end{bmatrix}.$$

Its z -domain transfer matrix is

$$G(z) = (z^2 I - A_1 z - A_2)^{-1} (B_0 z^2 + B_1 z + B_2), \quad (44)$$

6 and, elementwise,

$$[G(z)]_{ij} = \frac{b_{ij}^{(0)} z^2 + b_{ij}^{(1)} z + b_{ij}^{(2)}}{z^2 - a_i^{(1)} z - a_i^{(2)}}, \quad (45)$$

8 where $a_i^{(1)}$ and $a_i^{(2)}$ are the diagonal entries of A_1 and A_2 , respectively, and $b_{ij}^{(k)}$ are entries of B_k , where $k = 0, 1, 2$. A nonzero B_0 introduces direct feedthrough, making the system's relative degree to be zero in all input–output channels.

10 The denominator polynomials per output channel are

$$\begin{aligned} D_1(z) &= z^2 - 1.7z + 0.6, & p^{(1)} &= \{1.2, 0.5\} \quad (\text{unstable since } 1.2 > 1), \\ D_2(z) &= z^2 - 1.473z + 0.7225, & p^{(2)} &= \{0.737 \pm 0.424j\} \quad (|p| = 0.85 < 1), \\ D_3(z) &= z^2 - 1.8z + 0.81, & p^{(3)} &= \{0.9, 0.9\} \quad (\text{double pole}). \end{aligned}$$

Each transfer element $G_{ij}(z)$ has numerator $N_{ij}(z) = b_{ij}^{(0)} z^2 + b_{ij}^{(1)} z + b_{ij}^{(2)}$, yielding

$$\begin{aligned} G_{11} : z &= \{0, -0.25\}, & G_{12} : z &= \{\pm 0.7071\}, \\ G_{21} : z &= \{0, 0.25\}, & G_{22} : z &= \{0, -0.6667\}, \\ G_{31} : z &= \{\pm 0.8944\}, & G_{32} : z &= \{0, 0.2\}. \end{aligned}$$

12 All zeros satisfy $|z| < 1$ or $z = 0$. Hence, no NMP zeros are present. The initial conditions are $y_{-1} = y_{-2} = \mathbf{0}_3$, $u_{-2} = u_{-1} = u_0 = \mathbf{0}_2$.

This plant is linear, MIMO, and partially unstable (one mode outside the unit circle), with 2 nonzero direct feedthrough. It is used to demonstrate ABPC performance in a multivariable command-tracking setting, extending the previous SISO unstable example beyond stabilization.

4 All parameters are identical to Example 1, except that the system dimension is set to 5 $m = 2$, $p = 3$ (underactuated since $m < p$), the lag remains $\ell = 2$, the prediction horizon is 6 $N = 10$, and the input penalty is $R_u = 10^2 I$. Warm-up, excitation, and Q_y remain unchanged.

The reference sequence consists of three step commands:

$$r_k = \begin{cases} \begin{bmatrix} 1.0 & -0.5 & 2.0 \end{bmatrix}^\top, & k < 100, \\ \begin{bmatrix} -0.5 & 1.3 & -0.5 \end{bmatrix}^\top, & 100 \leq k < 200, \\ \begin{bmatrix} 0 & 0 & 0 \end{bmatrix}^\top, & k \geq 200. \end{cases}$$

8 Because the system is underactuated, these commands generally do not correspond to steady-state equilibria. At steady state, $y_{ss} = (I - A_1 - A_2)^{-1}(B_0 + B_1 + B_2)u_{ss}$, whose DC gain matrix 10 $G(1) \in \mathbb{R}^{3 \times 2}$ has rank 2. Hence, only references $r_{ss} \in \text{range } G(1)$ can be reached exactly. The 12 chosen step vectors lie outside this subspace; the responses instead follow a command-tracking-like profile reflecting projection onto the attainable output subspace.

The reported kernels are unitary, linear, and RBF. A degree-2 polynomial dictionary was 14 also tested under the same settings but proved numerically fragile: the larger parameterization increased the condition number of both the RLS covariance and the predictive Hessian, leading to 16 occasional loss of positive definiteness near the setpoint despite $R_u \succ 0$ and symmetry safeguards. This instability reflects variance and ill-conditioning under limited excitation, different from 18 the model-bias mechanism seen in Example 2b with sinusoidal disturbance. Therefore, the polynomial results are omitted, and the discussion focuses on the unitary, linear, and RBF cases.

20 Figure 9 shows that, despite one unstable mode and the system being underactuated, all 22 kernels yield bounded closed-loop responses that follow the step commands with clear command-tracking profiles. Transient speeds differ, with the linear kernel responding slowest, the RBF kernel fastest, and the unitary kernel showing the largest overshoot. The identification results 24 in Figure 10 confirm consistent parameter convergence across all kernels, with the unitary and RBF achieving faster error reduction than the linear kernel. The end-of-run heatmaps 26 in Figure 11 illustrate that all estimated coefficient matrices align closely with their true counterparts, demonstrating accurate RLS-based identification throughout the experiment.

Table 4 reports the total variation and peak magnitude of the control inputs after PRBS.

- 2 The results confirm that the unitary kernel produces the largest overall actuation and highest
- 4 peak input, consistent with its stronger overshoot observed in the output trajectories. The linear
- 6 kernel shows slightly lower total variation, while the RBF kernel achieves the smoothest control
- action with both the smallest TV_u and peak amplitude. These values align with the transient
- characteristics in Figure 9, where the RBF response is fastest yet least oscillatory.

Example 4. SISO Quadratic NARX without Cross Terms

2 Consider the discrete-time SISO system with lag $\ell = 2$

$$y_k = 1.5 y_{k-1} - 0.7 y_{k-2} + 0.5 u_k + 0.3 u_{k-1} \\ - 0.10 y_{k-1}^2 - 0.05 y_{k-2}^2 + 0.20 u_k^2 + 0.10 u_{k-1}^2. \quad (46)$$

4 Initial conditions: $y_{-1} = y_{-2} = u_0 = u_{-1} = 0$. The nonlinear terms are noncross: only squares
of individual regressors appear, without cross-products such as $y_{k-i}y_{k-j}$, $u_{k-i}u_{k-j}$, or $y_{k-i}u_{k-j}$.
The coefficients are chosen so that the linear backbone matches the baseline system of Example 1
6 and the even-order nonlinearities remain mild around the origin, keeping $y_k = 0$ an equilibrium.

8 This example introduces a controlled quadratic departure from linearity on both the
autoregressive and input channels while preserving the same memory and direct-feedthrough
structure. We apply ABPC and observe its behavior under these conditions.

10 The simulation setup follows the same configuration as in Example 1, using the same
reference signal defined in (39). All parameters, including horizon, forgetting factor, and
12 regularization, are kept identical to ensure comparability across examples. The only modification
is the input penalty, set to $\rho_u = 1$, which provides improved numerical conditioning for the
14 nonlinear case.

16 Figures 12–14 summarize the closed-loop and identification results for the quadratic SISO
NARX example. The output responses in Figure 12 show that the linear and polynomial kernels
achieve faster transients and smaller steady-state deviations than the unitary and RBF cases. The
18 corresponding one-step prediction errors in Figure 13 confirm the same trend, with the linear
and polynomial kernels sustaining the lowest residual levels across all commands. Despite their
20 lower accuracy, the unitary and RBF models remain numerically stable and do not diverge.

22 The estimated LPV-ARX blocks in Figure 14 further indicate bounded and coherent
parameter evolution for all kernels. In particular, the linear and polynomial coefficients fluctuate
around the nominal linear-part values and recover them at equilibrium, whereas the unitary and
24 RBF trajectories vary more slowly and remain farther from those landmarks.

26 To assess parameter accuracy, we compare the identified noncross coefficients with the true
quadratic NARX parameters for the linear and polynomial kernels. At each step k , the vector

$$\hat{\beta}_k = \theta_k[\mathcal{I}_{\text{true}}] \in \mathbb{R}^{10}, \quad \mathcal{I}_{\text{true}} = \{1, 2, 3, 4, 5, 6, 7, 13, 19, 25\},$$

28 collects the entries of θ_k that correspond, through the Kronecker construction of the regressor
 ϕ_k , to the monomials

$$\begin{bmatrix} 1 & y_{k-1} & y_{k-2} & u_k & u_{k-1} & u_{k-2} & y_{k-1}^2 & y_{k-2}^2 & u_k^2 & u_{k-1}^2 \end{bmatrix}^\top.$$

We define

$$\beta^* = \begin{bmatrix} 0 & 1.5 & -0.7 & 0.5 & 0.3 & 0 & -0.10 & -0.05 & 0.20 & 0.10 \end{bmatrix}^\top,$$

2 which contains the true system coefficients, including the intercept and the zero term on u_{k-2} .

All remaining parameters are grouped into a residual vector

$$\hat{\beta}_{\text{res},k} = \theta_k[\mathcal{I}_{\text{res}}], \quad \mathcal{I}_{\text{res}} = \{1, \dots, \dim(\theta_k)\} \setminus \mathcal{I}_{\text{true}},$$

4 and the corresponding residual norm $\|\hat{\beta}_{\text{res},k}\|_2$ is shown in logarithmic scale. Figure 15 displays
the evolution of $\hat{\beta}_k$ together with the residual norm, confirming that the identified coefficients

6 converge to the true values while the residuals vanish over time.

The quantitative results of Table 5 confirm the qualitative observations from Figures 12–15.

8 Linear and polynomial kernels achieve the lowest tracking errors and comparable input activity,
demonstrating near-identical performance. Unitary and RBF yield higher RMSE and IAE values,

10 with increased input variation and larger control peaks. Despite these differences, all methods
remain stable and bounded, consistent with the parameter behavior observed in Figure 14 and

12 15.

This example showed that, in a weakly nonlinear regime, the richer polynomial and linear

14 feature sets provide more accurate prediction and control while preserving numerical stability
across all kernels.

Example 5. SISO Polynomial Cross-Term Cubic NARX

2 Consider the discrete-time SISO system with lag $\ell = 2$

$$\begin{aligned} y_k &= 1.5 y_{k-1} - 0.7 y_{k-2} + 0.5 u_k + 0.3 u_{k-1} \\ &+ 6.5 y_{k-1} u_{k-1}^2 - 3.85 y_{k-2} u_{k-2}^2. \end{aligned} \quad (47)$$

Initial conditions are $y_{-1} = y_{-2} = u_0 = u_{-1} = u_{-2} = 0$. The nonlinear terms are degree-three cross monomials coupling past outputs with squared past inputs; no pure squares y_{k-i}^2 or u_{k-j}^2 appear. The coefficients preserve the linear backbone of Example 1 and maintain the origin as an equilibrium.

This example replaces the pure quadratic terms of Example 4 with cross terms of the form $y u^2$, providing a concise setting to assess kernel expressivity for mixed, higher-order interactions at fixed memory and direct feedthrough. A linear kernel cannot synthesize $u^2 y$ under the Kronecker construction (5), whereas a polynomial dictionary augmented with squared-input features can represent it exactly, and an RBF kernel can only approximate it. The unitary kernel is retained as a baseline; since it corresponds to the linear ARX structure, it lacks the expressivity to capture the cubic cross terms and serves only for reference. ABPC is applied to this system to evaluate its identification and tracking performance under this structured cross nonlinearity.

Figures 16–19 summarize the closed-loop results. The setup is identical to Example 4, except that the input penalty is increased to $R_u = 5 \times 10^{-2} I$ to maintain numerical stability of the Cholesky factorization; smaller values lead to near-singular matrices.

Figure 16 shows that all trajectories remain bounded and track the commands. The polynomial kernel consistently achieves the smallest tracking errors, followed by the linear kernel, while the unitary and RBF exhibit larger overshoots and steady-state deviations. The corresponding one-step prediction errors in Figure 17 confirm this hierarchy: during PRBS excitation, all kernels converge rapidly, but after PRBS the polynomial remains the most accurate and stable. The unitary and linear cases plateau at higher error levels as excitation diminishes, whereas the RBF error continues decreasing and reaches the lowest value at the end of the run.

Figure 18 reports the LPV–ARX coefficient evolution. All estimates are bounded and respond to command changes. The linear and polynomial kernels stay closest to the nominal linear coefficients 1.5 and -0.7 , while the unitary and RBF deviate more visibly. Finally, Figure 19 shows that the identified parameters corresponding to the linear part converge during PRBS and remain stable, whereas the cross coefficients move toward their true values without fully settling. The residual norm decreases sharply during PRBS and stabilizes at a low level toward the end.

To assess parameter accuracy, the identified vector

$$\hat{\beta}_k = \theta_k[\mathcal{I}_{\text{true}}] \in \mathbb{R}^8, \quad \mathcal{I}_{\text{true}} = \{1, 2, 3, 4, 5, 6, 47, 53\},$$

² collects the entries of θ_k corresponding to the monomials

$$\begin{bmatrix} 1 & y_{k-1} & y_{k-2} & u_k & u_{k-1} & u_{k-2} & y_{k-1}u_{k-1}^2 & y_{k-2}u_{k-2}^2 \end{bmatrix}^\top,$$

with the true vector

$$\beta^* = \begin{bmatrix} 0 & 1.5 & -0.7 & 0.5 & 0.3 & 0 & 6.5 & -3.85 \end{bmatrix}^\top.$$

⁴ All remaining parameters form the residual vector $\hat{\beta}_{\text{res},k} = \theta_k[\mathcal{I}_{\text{res}}]$, whose norm is shown in logarithmic scale.

⁶ The quantitative results in Table 6 are consistent with the qualitative observations in Figures 16–19. The polynomial kernel achieves the lowest tracking error in both RMSE and
⁸ IAE, confirming its ability to capture the cubic cross terms directly. The linear kernel follows with moderate accuracy, while the unitary and RBF yield the largest residuals, consistent with
¹⁰ their visible steady-state biases. All methods exhibit comparable control activity (TV_u and Peak_u remain within a narrow range), indicating that the improved accuracy of the polynomial case is
¹² not obtained at the cost of higher control effort. These results reinforce the conclusion that explicit polynomial features provide the most balanced performance for this nonlinear configuration.

Example 6. SISO Hammerstein Benchmark

2 Consider the discrete-time SISO Hammerstein system with lag $\ell = 2$

$$w_k = u_k + \alpha u_k^2 + \beta u_k^3, \quad (48)$$

$$y_k = 2.0 y_{k-1} - 1.01 y_{k-2} + 0.5 w_{k-1} - 0.65 w_{k-2}, \quad (49)$$

where $\alpha = 1.6$ and $\beta = 1.1$. Initial conditions are $y_{-1} = y_{-2} = w_{-1} = w_{-2} = u_{-1} = u_{-2} = 0$.

4 The nonlinearity (48) is a static cubic transformation of the input, while the subsequent dynamics
8 (49) are purely linear and identical to the unstable linear backbone used in Example 2.

6 This structure corresponds to the classical Hammerstein configuration [35], in which
a memoryless input nonlinearity precedes an LTI subsystem. Unlike the NARX model of
8 Example 5, the nonlinearity acts solely on the input channel and is separable from the system
dynamics, forming a block-oriented structure without feedback coupling. Such separation allows
10 an exact representation with polynomial kernels, while linear, RBF, and unitary kernels can
only approximate the static nonlinearity. The example thus serves as a standard benchmark to
12 assess ABPC performance on systems with input-side nonlinearities.

14 The same configuration as in Example 2 is used, except that the prediction horizon is
increased to $N = 30$ and the input penalty is set to $R_u = 10^3 I$ to ensure numerical stability.

16 The PRBS excitation window is slightly extended to $T_{\text{warm}} = 10$, and the reference sequence is
defined as

$$r_k = \begin{cases} 0.5, & k \in [11, 400], \\ 1.5, & k \in [401, 800], \\ 3.0, & k \in [801, 1200], \\ 0.0, & k > 1200. \end{cases}$$

18 All other parameters are identical to those of Example 2.

20 Figures 20 and 21 illustrate the closed-loop behavior of ABPC on the unstable Hammerstein
system. All kernels maintain bounded trajectories under the strong input nonlinearity. In output
22 tracking (Figure 20), the polynomial kernel achieves the most accurate responses across all
command steps, while the linear kernel remains moderate and the unitary and RBF exhibit larger
24 transients and residual errors. The one-step prediction errors (Figure 21) confirm this ranking:
polynomial lowest, linear intermediate, unitary and RBF highest during the early phases. As
26 excitation decreases in the final stabilization phase, the RBF continues to improve and ends with
the smallest residual error, consistent with its local approximation capability. Overall, the results

demonstrate the robustness of ABPC under unstable dynamics and strong input nonlinearities,
2 with kernel performance following the expected structural hierarchy.

The numerical results in Table 7 confirm the qualitative trends observed in Figures 20
4 and 21. The polynomial kernel attains the lowest RMSE and IAE, consistent with its accurate
6 representation of the cubic input nonlinearity. The linear kernel performs moderately, while the
8 unitary and RBF cases show larger tracking errors and accumulated deviations. Among them, the
10 unitary kernel yields the highest IAE, matching its visible undershoot and slower convergence.
Control activity metrics (TV_u , $Peak_u$) remain comparable across all kernels, indicating that the
improvement of the polynomial case is achieved without excessive input effort. These results
quantitatively reinforce the ranking inferred from the plots.

The same experiment is repeated in the Appendix to examine the robustness of ABPC.

Example 7. MIMO Nonlinear Application — Attitude Stabilization

2 Consider the attitude dynamics of a rigid body on $SO(3)$ represented by a unit quaternion
 $q = [\eta \ \varepsilon^\top]^\top \in \mathbb{R}^4$ ($\eta \in \mathbb{R}$, $\varepsilon \in \mathbb{R}^3$, $\|q\| = 1$) and body angular velocity $\omega \in \mathbb{R}^3$. The
4 continuous-time equations are

$$\dot{q} = \frac{1}{2} \Omega(\omega) q, \quad (50)$$

$$J \dot{\omega} = \tau - \omega \times (J\omega), \quad (51)$$

where $J \in \mathbb{R}_{>0}^{3 \times 3}$ is the inertia matrix, $\tau \in \mathbb{R}^3$ is the control torque, and

$$\Omega(\omega) = \begin{bmatrix} 0 & -\omega^\top \\ \omega & -[\omega]_\times \end{bmatrix},$$

6 with $[\omega]_\times$ the skew-symmetric matrix satisfying $[\omega]_\times x = \omega \times x$.

For a simulation with sampling period $T_s > 0$, a unit-norm-preserving quaternion update
8 via the exponential map is used. Define

$$\theta_k := \|\omega_k\| T_s, \quad (52)$$

$$\text{sinc}(x) := \begin{cases} \frac{\sin x}{x}, & x \neq 0, \\ 1, & x = 0, \end{cases} \quad (53)$$

$$\Delta q_k := \begin{bmatrix} \cos\left(\frac{\theta_k}{2}\right) \\ \frac{T_s}{2} \text{sinc}\left(\frac{\theta_k}{2}\right) \omega_k \end{bmatrix}, \quad (54)$$

and the Hamilton product $p \otimes q$ by

$$\begin{bmatrix} \eta_p \\ \varepsilon_p \end{bmatrix} \otimes \begin{bmatrix} \eta_q \\ \varepsilon_q \end{bmatrix} = \begin{bmatrix} \eta_p \eta_q - \varepsilon_p^\top \varepsilon_q \\ \eta_p \varepsilon_q + \eta_q \varepsilon_p + \varepsilon_p \times \varepsilon_q \end{bmatrix}. \quad (55)$$

10 Then the discrete-time dynamics are

$$q_{k+1} = \Delta q_k \otimes q_k, \quad (56)$$

$$\omega_{k+1} = \omega_k + T_s J^{-1}(\tau_k - \omega_k \times (J\omega_k)), \quad (57)$$

where $\|q_{k+1}\| = 1$ by construction. For numerical precision, re-normalize $q_{k+1} \leftarrow q_{k+1} / \|q_{k+1}\|$
12 to counter floating-point round-off.

The measured output is composed of the quaternion error and the body angular velocity.

14 At each sampling instant, the desired and actual attitudes $q_{d,k}$ and q_k yield $\tilde{q}_k = q_{d,k}^{-1} \otimes q_k$, with sign convention $\tilde{\eta}_k \geq 0$. The output vector is

$$y_k = \begin{bmatrix} \tilde{\varepsilon}_k \\ \omega_k \end{bmatrix} \in \mathbb{R}^6,$$

where $\tilde{\varepsilon}_k$ is the vector part of \tilde{q}_k and ω_k is the measured body angular rate. This formulation
2 eliminates quaternion sign ambiguity and unit-norm redundancy while retaining full attitude
information.

4 Initial conditions: $q_0 = [0.95 \ -0.04 \ 0.17 \ 0.25]^\top$, $\omega_0 = \mathbf{0}_3$ rad/s. This MIMO nonlinear
model is used to assess ABPC on $SO(3)$ with quaternion kinematics and rigid-body dynamics.
6 We use $J = \text{diag}\{0.5, 1.5, 1\}$ kg·m² and $T_s = 0.05$ s. The setup is identical to Example 3 except
for the system dimensions and control horizon. Here, the plant has $m = 3$ inputs and $p = 6$
8 outputs with lag $\ell = 1$ across all kernels. The warm-up period is $T_{\text{warm}} = 100$ steps = 5 s, and
10 the identification parameters (λ , ridge, and numerical tolerances) are unchanged. The control
horizon is extended to $N = 30$ steps = 1.5 s, while the input penalty is reduced to $\rho_u = 10^{-2}$;
all other configurations remain identical to Example 3.

12 Although the linear and polynomial kernels appear to converge more slowly in the time-
domain plots (see Figure 22), their steady-state tracking accuracy (as reported by RMSE and
14 IAE in Table 8) is superior. This difference arises because the performance metric also includes
the angular-velocity components within the output vector, and the linear and polynomial kernels
16 generate smoother responses with smaller velocity amplitudes. Consequently, their trajectories
remain closer to the reference (which is zero for both attitude and angular rate) despite slower
18 transient convergence. The unitary and RBF kernels reach the equilibrium faster but with slightly
larger velocity excursions, leading to higher integrated error. All methods maintain comparable
20 control effort (TV_u , Peak_u), confirming that the observed accuracy differences result from the
trade-off between transient speed and overall output smoothness.

Conclusion

2 This study presented ABPC, a kernel-based indirect adaptive controller that identifies an
3 LPV-ARX one-step predictor online with kernel-RLS, stacks predictions over a finite horizon,
4 and computes the control sequence in closed form via Cholesky. The method operates on
5 streaming data without batch Hankel matrices or iterative QPs. Across numerical examples,
6 performance is strong when the kernel dictionary aligns with the plant class (Hammerstein,
7 NARX with and without cross terms, polynomial, cubic, quaternion), while fragility appears
8 for sinusoidal content represented by polynomial features; the unitary dictionary mitigates this
9 through the internal-model effect. In linear regimes, RBF features occasionally outperform the
10 unitary baseline. The per-step computation is dominated by a Cholesky factorization of size
11 $mN \times mN$, with memory $O((mN)^2)$. Results are numerical and reproducible; formal stability
12 and robustness analysis for the frozen surrogate is left open.

Future work targets constrained control and adaptation under abrupt changes. For constraints, we will study closed-form or near-closed-form treatments such as soft-penalty schedules, projections, and factor-updated active-set methods. For fast transients, variable-rate forgetting and change-detection resets will be combined with kernel dictionaries that are sparsified and pruned to reduce numerical fragility and parameter count. We also plan to formalize conditions that connect dictionary expressiveness, persistence of excitation, rank/conditioning of stacked operators, and bounds on coefficient drift across the horizon, and to report implementations with complete configurations for full reproducibility.

Appendix

2 Proof of Lemma 1 (Stacked LPV–ARX Propagation)

Proof. Let $E_j \in \mathbb{R}^{p \times pN}$ select the j -th output block so that $E_j Y = y_{j|k}$. By construction,

$$E_j(S_i \otimes A_{k,i})Y = \begin{cases} A_{k,i}y_{j-i|k}, & j > i, \\ 0, & j \leq i, \end{cases} \quad (58)$$

$$E_j(S_i \otimes B_{k,i})U = \begin{cases} B_{k,i}u_{j-i|k}, & j > i, \\ 0, & j \leq i. \end{cases} \quad (59)$$

4 For the known initial conditions, F_i selects the first i rows. Hence,

$$E_j(F_i \otimes A_{k,i})Y_{\text{init}}^{(i)} = \begin{cases} A_{k,i}y_{k+j-i}, & j \leq i, \\ 0, & j > i, \end{cases} \quad (60)$$

$$E_j(F_i \otimes B_{k,i})U_{\text{init}}^{(i)} = \begin{cases} B_{k,i}u_{k+j-i}, & j \leq i, \\ 0, & j > i. \end{cases} \quad (61)$$

Therefore, the j -th block row of $(I_{pN} - T_y)Y = \sigma_k + T_u U$ reads

$$y_{j|k} - \sum_{i=1}^{\min\{\ell, j-1\}} A_{k,i}y_{j-i|k} = C_k + \sum_{i=0}^{\min\{\ell, j-1\}} B_{k,i}u_{j-i|k} + \sum_{i=j}^{\ell} (A_{k,i}y_{k+j-i} + B_{k,i}u_{k+j-i}), \quad (62)$$

6 which is, by definition, the LPV–ARX recursion: use predicted outputs when $j - i \geq 1$ and measured (y_{k+j-i}, u_{k+j-i}) when $j \leq i$. Since this holds for all $j = 1, \dots, N$, the stacked identity
8 follows. Note that T_y is strictly block lower triangular. Therefore, $T_y^N = 0$ and the Neumann series gives $(I_{pN} - T_y)^{-1} = \sum_{r=0}^{N-1} T_y^r$ [36]. Substitution yields $Y = S_k + G_k U$. \square

Example 2b. Robustness Test

2 This section repeats the frequency-domain test of Example 2b under additive measurement
3 noise. A zero-mean Gaussian perturbation ν_k with standard deviation $\sigma_{\text{noise}} = 10^{-2}$ is added
4 to the measured output y_k . All other parameters are identical to the noiseless case: disturbance
5 amplitude $A = 0.01$, lag order $\ell = 5$, and frequency sweep $\omega \in [0, \pi]$ with step 0.05. Performance
6 is evaluated over the same period-aligned windows, and the logarithmic RMSE is plotted as a
7 function of ω . All performance metrics are computed using the noise-free output y_k , not the
8 measured signal $y_{n,k} = y_k + \nu_k$.

9 As shown in Figure 23, both kernels remain bounded across all frequencies and preserve
10 the general attenuation pattern observed in the noiseless case. The RBF and unitary kernels now
11 exhibit comparable performance, with the RBF curve lying slightly above the unitary over most
12 of the band, indicating a small but consistent loss of suppression under noisy measurements.

Example 6. Robustness Test

2 This section repeats the command-tracking experiment of Example 6 under additive
3 measurement noise. A zero-mean Gaussian perturbation ν_k with standard deviation $\sigma_{\text{noise}} = 10^{-3}$
4 is added to the measured output. All other parameters are identical to the noiseless case, except
5 that the forgetting factor is set to $\lambda = 0.999$, the ridge parameter is increased to $\rho = 10^{-4}$, the
6 prediction horizon is extended to $N = 30$, and the input penalty is raised to $R_u = 2.25 \times 10^4 I$
7 for numerical stability. Only the output response is displayed, as the logarithmic error becomes
8 visually dominated by the noise. All performance metrics are computed with respect to the
noise-free output y_k , not the measured signal $y_{n,k} = y_k + \nu_k$.

10 Figure 24 shows the simulation results for the robustness test. Quantitatively, the ranking
11 of the kernels remains consistent with the noiseless case: the polynomial kernel achieves the
12 lowest RMSE and IAE, followed by the linear kernel, while the unitary and RBF exhibit larger
13 tracking errors. The relative increase in all error measures confirms the effect of measurement
14 noise, yet all trajectories remain bounded and stable. Control activity indicators (TV_u , $Peak_u$)
15 remain comparable across kernels, showing that the polynomial maintains its accuracy without
16 increased input effort. These quantitative results confirm the trends observed visually in Figure 24.

References

[1] J. C. Willems and J. W. Polderman, *Introduction to mathematical systems theory: a behavioral approach*. Springer Science & Business Media, 1997, vol. 26.

[2] M. Morari and J. H. Lee, “Model predictive control: Past, present and future,” *Computers & chemical engineering*, vol. 23, no. 4-5, pp. 667–682, 1999.

[3] F. Allgöwer and A. Zheng, *Nonlinear model predictive control*. Birkhäuser, 2012, vol. 26.

[4] J. B. Rawlings, D. Q. Mayne, M. Diehl, et al., *Model predictive control: theory, computation, and design*. Nob Hill Publishing Madison, WI, 2020, vol. 2.

[5] I. Markovsky, J. C. Willems, S. Van Huffel, B. De Moor, and R. Pintelon, “Application of structured total least squares for system identification and model reduction,” *IEEE Transactions on Automatic Control*, vol. 50, no. 10, pp. 1490–1500, 2005.

[6] J. Coulson, J. Lygeros, and F. Dörfler, “Data-enabled predictive control: In the shallows of the DeePC,” in *2019 18th European Control Conference (ECC)*, 2019, pp. 307–312. DOI: [10.23919/ECC.2019.8795639](https://doi.org/10.23919/ECC.2019.8795639)

[7] J. Berberich, J. Köhler, M. A. Müller, and F. Allgöwer, “Data-driven model predictive control with stability and robustness guarantees,” *IEEE transactions on automatic control*, vol. 66, no. 4, pp. 1702–1717, 2020.

[8] G. C. Goodwin, M. E. Salgado, and R. H. Middleton, “Indirect adaptive control: An integrated approach,” in *1988 American Control Conference*, IEEE, 1988, pp. 2440–2445.

[9] K. J. Astrom and B. Wittenmark, *Adaptive control*. Addison-Wesley Longman Publishing Co., Inc., 1994.

[10] L. Ljung, “System identification,” in *Signal analysis and prediction*, Springer, 1998, pp. 163–173.

[11] A. A. Feldbaum, “Dual control theory. I,” *Avtomatika i Telemekhanika*, vol. 21, no. 9, pp. 1240–1249, 1960.

[12] D. W. Moore and E. A. Spiegel, “A thermally excited non-linear oscillator,” *Astrophysical Journal*, vol. 143, p. 871, vol. 143, p. 871, 1966.

[13] M. Green and J. B. Moore, “Persistence of excitation in linear systems,” *Systems & control letters*, vol. 7, no. 5, pp. 351–360, 1986.

[14] Y. Rahman, A. Xie, and D. S. Bernstein, “Retrospective cost adaptive control: Pole placement, frequency response, and connections with LQG control,” *IEEE Control Systems Magazine*, vol. 37, no. 5, pp. 28–69, 2017.

[15] B. Y. Lai, S. A. U. Islam, S. Nivison, and D. S. Bernstein, “Data-driven retrospective cost adaptive control of a quadrotor UAV,” in *AIAA SCITECH 2023 Forum*, 2023, p. 0694.

[16] N. Mohseni and D. S. Bernstein, “Retrospective cost adaptive harmonic disturbance rejection using dereverberated target models,” *Journal of Sound and Vibration*, vol. 523, p. 116692, 2022.

[17] T. W. Nguyen, S. A. U. Islam, D. S. Bernstein, and I. V. Kolmanovsky, “Predictive cost adaptive control: A numerical investigation of persistency, consistency, and exigency,” *IEEE Control Systems Magazine*, vol. 41, no. 6, pp. 64–96, 2021.

[18] D. W. Clarke, C. Mohtadi, and P. S. Tuffs, “Generalized predictive control—part I. the basic algorithm,” *Automatica*, vol. 23, no. 2, pp. 137–148, 1987.

[19] D. W. Clarke, C. Mohtadi, and P. S. Tuffs, “Generalized predictive control—part II extensions and interpretations,” *Automatica*, vol. 23, no. 2, pp. 149–160, 1987.

[20] D. W. Clarke and C. Mohtadi, “Properties of generalized predictive control,” *Automatica*, vol. 25, no. 6, pp. 859–875, 1989.

[21] D. W. Clarke, “Application of generalized predictive control to industrial processes,” *IEEE Control systems magazine*, vol. 8, no. 2, pp. 49–55, 2002.

[22] R. J. Richards, S. A. U. Islam, and D. S. Bernstein, “Predictive cost adaptive control of the NASA benchmark flutter model,” *Journal of Guidance, Control, and Dynamics*, pp. 1–17, 2025.

[23] R. J. Richards, J. A. Marshall, and D. S. Bernstein, “Experimental flight testing a quadcopter autopilot based on predictive cost adaptive control,” in *2025 American Control Conference (ACC)*, IEEE, 2025, pp. 2471–2476.

[24] J. C. Vander Schaaf, R. Acharya, and D. Bernstein, “Predictive cost adaptive control of shock-boundary-layer interaction in a scramjet inlet,” *Physics of Fluids*, vol. 37, pp. 086170–086186, 2025.

[25] D. Serbin, K. Fidkowski, and D. Bernstein, “Predictive cost adaptive control of 3DOF CFD-simulated flight,” in *AIAA SCITECH 2025 Forum*, 2025, p. 2466.

[26] T. W. Nguyen, I. V. Kolmanovsky, and D. S. Bernstein, “Sampled-data output-feedback model predictive control of nonlinear plants using online linear system identification,” in *2021 American Control Conference (ACC)*, IEEE, 2021, pp. 4692–4697.

[27] I. Markovsky and F. Dörfler, “Behavioral systems theory in data-driven analysis, signal processing, and control,” *Annual Reviews in Control*, vol. 52, pp. 42–64, 2021.

[28] B. A. Francis and W. M. Wonham, “The internal model principle of control theory,” *Automatica*, vol. 12, no. 5, pp. 457–465, 1976.

[29] J. C. Willems, “Paradigms and puzzles in the theory of dynamical systems,” *IEEE Transactions on automatic control*, vol. 36, no. 3, pp. 259–294, 1991.

[30] A. Simpkins, “System identification: Theory for the user, 2nd edition (Ljung, L.; 1999),” *IEEE Robotics & Automation Magazine*, vol. 19, no. 2, pp. 95–96, 2012. DOI: [10.1109/MRA.2012.2192817](https://doi.org/10.1109/MRA.2012.2192817)

[31] S. A. Billings, *Nonlinear system identification: NARMAX methods in the time, frequency, and spatio-temporal domains*. John Wiley & Sons, 2013.

[32] B. Schölkopf and A. J. Smola, *Learning with kernels: support vector machines, regularization, optimization, and beyond*. MIT press, 2002.

[33] Y. Susuki, A. Mauroy, and Z. Drmač, “Koopman resolvents of nonlinear discrete-time systems: Formulation and identification,” in *2024 European Control Conference (ECC)*, IEEE, 2024, pp. 627–632.

[34] B. Lai, D. Panagou, and D. S. Bernstein, “Recursive least squares with fading regularization for finite-time convergence without persistent excitation,” *arXiv preprint arXiv:2501.04566*, 2025.

[35] S. Billings and S. Fakhouri, “Identification of systems containing linear dynamic and static nonlinear elements,” *Automatica*, vol. 18, no. 1, pp. 15–26, 1982, ISSN: 0005-1098. DOI: [https://doi.org/10.1016/0005-1098\(82\)90022-X](https://doi.org/10.1016/0005-1098(82)90022-X) [Online]. Available: <https://www.sciencedirect.com/science/article/pii/000510988290022X>

[36] D. S. Bernstein, *Theory, Facts, and Formulas — Revised and Expanded Edition*. Princeton: Princeton University Press, 2018, ISBN: 9781400888252. DOI: [doi:10.1515/9781400833344](https://doi.org/10.1515/9781400833344) [Online]. Available: <https://press.princeton.edu/books/paperback/9780691176536/scalar-vector-and-matrix-mathematics>

List of Figures

2 1	Example 1. Closed-loop output response of the four kernel configurations. Subplots (a)–(b) display the full and zoomed responses to the piecewise-constant reference signal (black dashed-line). The output trajectories for the unitary, linear, and radial-basis-function (RBF) kernels overlap, while the polynomial case initially shows a slight transient deviation for the first step command. Subplot (c) shows the absolute tracking error $ r_k - y_k $ on a logarithmic scale. All configurations track the reference sequence with progressively smaller error. At the final command step, the steady-state errors are approximately 2.2×10^{-16} (RBF), 2.9×10^{-12} (unitary), 4.6×10^{-11} (linear), and 6.6×10^{-11} (polynomial).	47
2	Example 1. One-step prediction error magnitude. The figure shows the instantaneous prediction error $ \hat{y}_k - y_k $ in logarithmic scale for all kernel configurations. During the pseudo-random binary sequence (PRBS) excitation phase, all errors decrease progressively, with more pronounced transient spikes for the linear and polynomial kernels. At each command step change, short error spikes reappear for all configurations, most noticeably for the polynomial case. The radial-basis-function (RBF) kernel converges rapidly and plateaus early, remaining the least accurate overall but reaching a final prediction error of approximately 10^{-14} . The unitary kernel maintains the most consistent accuracy, with a final error of about 2.8×10^{-12} , while the linear kernel performs comparably, ending near 4.5×10^{-11} . The polynomial kernel shows larger residuals, reaching around 6.4×10^{-11} at the end of the experiment.	48
3	Example 1. Identified linear-parameter-varying–autoregressive-with-exogenous-input (LPV–ARX) coefficients over time. Each panel shows the estimated $A_{k,j}$, $B_{k,j}$, and C_k compared with the true parameters (dashed black). Across all kernels, the identified coefficients approach the true values after a short transient. For the A_k blocks, the unitary and radial-basis-function (RBF) kernels reach the steady level within a few steps, while the linear and polynomial kernels exhibit slower transients. When zoomed in, small fluctuations appear for the polynomial kernel around the first two command changes, indicating slightly higher sensitivity to excitation; no further variations occur afterward. A similar trend appears in B_k : both unitary and RBF responses stabilize rapidly, while the polynomial case exhibits mild fluctuations around the first two command changes. The RBF shows a slower adjustment in $B_{k,2}$ than the unitary. For the intercept C_k , all kernels evolve smoothly toward the same steady value. The RBF remains at zero throughout, while the others converge with comparable speed and without visible fluctuations.	49

4	Example 2a. Closed-loop output response of the four kernel configurations. (a) All kernels start with a small overshoot followed by a negative excursion before recovering. The recovery order is radial basis function (RBF), unitary, linear, and polynomial. All responses reach stabilization, but oscillation amplitude increases in the same order, with approximate second-peak magnitudes of 0.35 (RBF), 0.54 (unitary), 0.67 (linear), and 1.26 (polynomial). The oscillation period is approximately 40 steps for all kernels. (b) Logarithmic squared-error traces with respect to the origin. Error magnitudes decrease after the PRBS phase, consistent with the attenuation of oscillations observed in (a). The same performance ranking is maintained: RBF lowest, followed by unitary, linear, and polynomial. Small envelope-like periodic modulations reflect the residual oscillatory component of the output.	50
5	Example 2a. Linear-parameter-varying-autoregressive-with-exogenous-input (LPV-ARX) coefficient evolution for $k \in [0, 60]$. (a) A_k : The radial-basis-function (RBF) and unitary kernels reach the true value within the pseudo-random binary sequence (PRBS) window and remain close thereafter. The linear kernel reaches the true value with moderate fluctuations and settles by about 20 steps. The polynomial kernel reaches the true value with larger fluctuations and settles by about 45 steps. Beyond 60 steps, all traces are steady; the complete history curves are omitted for clarity. (b) B_k : Similar trend. RBF and unitary settle within roughly 10 steps (about 5 steps after the 5-step PRBS). Linear settles more slowly, while polynomial shows wider fluctuations and stabilizes by about 45 steps. Beyond 60 steps all traces remain steady. (c) C_k : For the RBF kernel the intercept is already captured, yielding $C_k \equiv 0$. Unitary approaches zero within about 10 steps, linear by about 25 steps, and polynomial by about 45 steps.	51
6	Example 2b (Unitary kernel). (a) Output responses y_k and (b) logarithmic instantaneous output energy $\log_{10}(y_k^2)$ are shown for a fixed disturbance frequency $\omega = \pi/4$. Each row corresponds to a disturbance amplitude $A \in \{0.1, 0.5, 1\}$, and, within each row, the lag order increases from $\ell = 2$ to $\ell = 5$. Across all amplitudes, the most pronounced transients occur for $\ell = 3$, lasting roughly 300 steps, as visible in both the time and logarithmic scales. Overall, $\ell = 2$ and $\ell = 3$ exhibit the largest transient amplitudes, while the smoothest and fastest settling responses are obtained for $\ell = 5$. At steady state, $\ell = 2$ consistently shows the highest residual level, remaining above all other traces from steps 350 to 500. For $A = 0.1$ and $A = 0.5$, $\ell = 3$ achieves suppression comparable to $\ell = 4$ and $\ell = 5$, whereas at $A = 1$ a small steady-state offset persists. The lowest and most stable steady-state energy levels are observed for $\ell = 4$ and $\ell = 5$, with no apparent drift over time. Linear and polynomial kernels are not shown here; their responses diverge under harmonic disturbance due to parameter chasing (see main text). These results indicate that increasing ℓ reinforces the internal-model effect in the AR structure, allowing the unitary dictionary under online RLS to capture the sinusoidal mode and achieve effective suppression at higher orders.	52

Example 2b (Radial-basis-function (RBF) kernel). (a) Output responses y_k and (b) logarithmic instantaneous output energy $\log_{10}(y_k^2)$ are shown for a fixed disturbance frequency $\omega = \pi/4$. Each row corresponds to a disturbance amplitude $A \in \{0.1, 0.5, 1\}$, and, within each row, the lag order increases from $\ell = 2$ to $\ell = 5$. Across all amplitudes, $\ell = 3$ consistently produces the largest transient, as visible in both the time and logarithmic scales. For $A = 0.5$ and $A = 1$, the corresponding trajectories diverge exponentially, confirmed by the sustained high levels of $\log_{10}(y_k^2)$. When $\ell = 2$, the disturbance is not effectively suppressed in any case: at $A = 0.1$ the output trajectory slowly drifts downward, at $A = 0.5$ it remains bounded but with large steady oscillations, and at $A = 1$ the amplitude grows unbounded. In contrast, for $\ell = 4$ and $\ell = 5$ the oscillations are markedly attenuated and the steady-state energy remains low and stable across all amplitudes. At $A = 0.1$, the $\ell = 2$ trace approaches a similar steady level to $\ell = 4$ and $\ell = 5$, though with a slower and less regular transient. Taken together, these results indicate that, with the RBF kernel, effective disturbance rejection emerges only for higher lag orders, typically $\ell \geq 4$, which is greater than required in the unitary case. This suggests that the RBF basis models the sinusoidal disturbance accurately once sufficient dynamic depth is provided by the autoregressive structure.

Example 2b. Frequency-domain disturbance analysis. The disturbance amplitude is fixed at $A = 0.01$ and the lag order at $\ell = 5$. For each $\omega \in [0, \pi]$, performance is evaluated over the last $T_\omega = \lceil 2\pi/\omega \rceil$ samples of a 5000-step run, while for $\omega = 0$ a fixed 1000-sample window is used. The plotted quantity is the logarithmic root-mean-square error (RMSE) evaluated over the period-aligned windows. Both kernels remain bounded over the entire frequency range and effectively reduce the disturbance energy. Their responses approximately coincide at low frequency, but diverge as ω increases, where the radial-basis-function (RBF) kernel achieves consistently lower output energy than the unitary case. See Appendix for robustness test.

Example 3. Closed-loop responses for the underactuated multi-input multi-output (MIMO) system ($m = 2, p = 3$) using unitary, linear, and radial-basis-function (RBF) kernels. Although the open-loop plant contains one unstable mode, all three kernels produce bounded and well-behaved closed-loop trajectories. Each output exhibits a command-tracking-like evolution rather than exact convergence, consistent with the limited steady-state reachability implied by rank $G(1) = 2 < 3$. Transient behavior differs across kernels: the linear kernel yields the slowest response, the RBF kernel responds fastest with minimal overshoot, and the unitary kernel shows the largest overshoot and undershoot before settling. Across all kernels, $y_{k,3}$ follows the reference accurately for all commands. During the first step, $y_{k,1}$ approaches its target with a small steady-state error, while $y_{k,2}$ settles around -0.06 instead of the commanded -0.5 , leaving a clear residual offset. In the second step, $y_{k,3}$ again tracks closely, whereas the first and second outputs remain bounded but retain finite tracking errors. For the final command ($r_k = 0$), all outputs decay smoothly with minimal residual error, confirming closed-loop boundedness under all kernels.

10 11 **Example 3.** End-of-run parameter heatmaps for A_1 , A_2 , B_0 , B_1 , B_2 , and the
 12 intercept $C \equiv 0$. Rows correspond, in order, to the linear, unitary, radial-basis-
 14 function (RBF), and true matrices. All kernels yield coefficient matrices visually
 16 close to the true ones, confirming consistent convergence of the recursive-least-
 squares (RLS) identification. For the intercept block C , the linear kernel produces
 a nearly zero matrix with residual elements on the order of 10^{-9} , while the unitary
 and RBF kernels remain close to or exactly zero. Overall, all identified coefficients
 align well with the true values, indicating accurate parameter recovery. 57

13 **Example 4.** One-step prediction error. The prediction error $|\hat{y}_k - y_k|$ is computed in a predictive framework with $\hat{y}_k = \phi_k \theta_k$, using the pre-update (*a-priori*) parameter estimate θ_k rather than the *a-posteriori* θ_{k+1} . During the pseudo-random binary sequence (PRBS) phase, the polynomial and linear kernels exhibit two pronounced transient spikes but achieve the largest overall decrease in prediction error. For each step command, the polynomial kernel shows sharper spikes yet rapidly converges, while the linear kernel attains the lowest steady values (approximately 10^{-11} with terminal plateaus near 2×10^{-11}). The polynomial follows with decreasing plateaus for successive steps, reaching about 2.3×10^{-10} . In contrast, the radial-basis-function (RBF) and unitary kernels remain less accurate, with plateau ranges between 4×10^{-3} and 2×10^{-2} across the steps. During the stabilization phase ($r_k \equiv 0$), the unitary kernel yields the poorest accuracy ($|e_k| \approx 0.022$), while the RBF error decreases nearly linearly in the logarithmic scale and gradually approaches the polynomial and linear levels.

59

14 **Example 4.** Estimated linear-parameter-varying–autoregressive-with-exogenous-input (LPV–ARX) blocks $\{A_k, B_k, C_k\}$. The coefficient trajectories remain bounded with no visible drift or divergence. After each step, the linear and polynomial kernels change sharply and settle quickly, while unitary and radial basis function (RBF) evolve more slowly. The nominal linear part is $1.5 y_{k-1} - 0.7 y_{k-2} + 0.5 u_k + 0.3 u_{k-1}$. In A_k , entries $A_{k,1}$ and $A_{k,2}$ oscillate around 1.5 and -0.7 for linear/polynomial and stay in the same vicinity for unitary/RBF. This proximity likely reflects mild nonlinear effects producing small biases. In B_k , $B_{k,0}$ and $B_{k,1}$ cluster near 0.5 and 0.3 for linear/polynomial, whereas unitary/RBF deviate; the extra lag term $B_{k,2}$ is near zero only for linear/polynomial. For C_k , the linear/polynomial traces approach zero, the RBF is fixed at zero, and the unitary remains negative. During stabilization ($r_k \equiv 0$), the linear/polynomial coefficients recover the nominal linear-part values within numerical precision.

60

28 15 **Example 4.** Coefficient recovery for linear and polynomial kernels. We observe
 29 that the identified coefficients approach the true values in all cases. For components
 30 $\hat{\beta}_{k,1:8}$, most convergence occurs during the pseudo-random binary sequence (PRBS)
 31 phase. The last two components ($\hat{\beta}_{k,9:10}$) converge sharply at the onset of step
 32 commands: the linear kernel settles immediately after PRBS ($k \approx 60$), whereas the
 33 polynomial kernel converges more gradually, stabilizing near $k \approx 170$. The residual
 34 norm decreases in both cases, abruptly after the first command for the linear kernel
 35 and in a stepwise manner for the polynomial one, with the polynomial maintaining a
 36 slightly higher final residue ($\log_{10} \|\hat{\beta}_{\text{res},k}\| \approx -6.7$) than the linear kernel (≈ -8.3)

61

62

63

18	Example 5. Linear-parameter-varying-autoregressive-with-exogenous-input (LPV-ARX) coefficient evolution. All estimated coefficients remain bounded and respond to command changes. For $A_{k,1}$, the linear and polynomial kernels stay closest to the nominal linear coefficient 1.5 (the true value associated with y_{k-1} in the linear backbone of the cubic nonlinear autoregressive-with-exogenous-input (NARX) model), whereas the unitary and radial basis function (RBF) deviate more. For $A_{k,2}$, all trajectories oscillate around the nominal value -0.7 , corresponding to the coefficient of y_{k-2} in the same linear backbone. The B_k coefficients remain bounded, with the largest variations observed for the linear and polynomial cases. All C_k terms stay near zero, the linear kernel showing the largest offset. These bounded oscillations and coefficient shifts are consistent with the excitation of nonlinear components and structure-dependent sensitivity.	64
19	Example 5 (Polynomial case only). Identified parameters at indices aligned with the true parameterization. During pseudo-random binary sequence (PRBS), the linear-part coefficients $\hat{\beta}_{k,1:6}$ move toward their true values and remain close thereafter. In the control phase, the cross coefficients evolve: $\hat{\beta}_{k,7}$ rises toward 6.5 but ends at 5.06; $\hat{\beta}_{k,8}$ drops near -3.85 early, then overshoots and ends at -4.43 . The residual decreases markedly during PRBS, increases around the first step, decreases again around the third step, and settles near -4.2 (log scale) by the end. Note that the near-zero values of $\hat{\beta}_{k,7:8}$ during PRBS are consistent with limited excitation of the cubic cross features.	65
20	Example 6. Output tracking and logarithmic error. All kernels remain bounded throughout the simulation. For the first step ($r_k = 0.5$), the unitary kernel exhibits the largest overshoot and slowest convergence, followed by the radial basis function (RBF) with a milder transient. The linear and polynomial kernels show smaller overshoots, with residual errors of 5.2×10^{-5} and 1.47×10^{-7} , respectively, while the unitary and RBF settle around 0.06 and 0.02. As the command increases to $r_k = 1.5$, the nonlinear influence strengthens: the polynomial overshoots most but, with the linear kernel, achieves the smallest steady-state error; RBF and unitary remain less accurate. At $r_k = 3$, the nonlinear distortion dominates; the linear kernel oscillates and gradually damps, while the polynomial tracks more closely despite mild oscillations. RBF and linear exhibit the largest deviations (≈ 0.3). In the final stabilization phase ($r_k \equiv 0$), all trajectories stay bounded; the unitary shows a persistent undershoot, and both polynomial and RBF display monotonic error decay, the RBF ending with the smallest final error by the end of the simulation.	66
21	Example 6. One-step prediction error in logarithmic scale. For the first three command steps, the unitary and radial-basis-function (RBF) kernels yield the poorest prediction accuracy, their traces remaining close throughout. They are followed by the linear kernel, while the polynomial consistently attains the lowest errors across all steps, reflecting its ability to represent the cubic input nonlinearity more accurately. During the final stabilization phase, the unitary kernel still plateaus at a high level, whereas the RBF error decays linearly and ends as the smallest among all kernels.	67

22	Example 7: Closed-loop quaternion trajectories with a fixed desired attitude $q_d = [1 \ 0 \ 0 \ 0]^\top$. The unitary and radial-basis-function (RBF) kernels exhibit a first-order-like transient response characterized by a nonzero initial slope followed by exponential-type convergence toward the commanded equilibrium. Across all quaternion components, the unitary and RBF responses nearly coincide throughout both transient and steady-state phases, indicating that the two parameterizations capture the local attitude dynamics equivalently. The polynomial kernel displays a slightly faster settling in ε_2 , whereas for the remaining components the polynomial and linear kernels converge more slowly.	68
10 23	Example 2b (Robustness test). Frequency-domain disturbance test repeated under additive Gaussian noise with standard deviation $\sigma_{\text{noise}} = 10^{-2}$. All other parameters are identical to the noiseless case ($A = 0.01$, $\ell = 5$, and $\omega \in [0, \pi]$ with step 0.05). The plotted quantity is the logarithmic root-mean-square error (RMSE) of the noise-free output y_k evaluated over the period-aligned windows. Both kernels remain bounded across all frequencies and preserve the qualitative attenuation pattern observed in the noiseless experiment. Their curves now lie close to each other, with the radial-basis-function (RBF) trace slightly above the unitary over most of the band, indicating comparable but marginally weaker suppression in the presence of noise.	69
20 24	Example 6 (Robustness test). Output tracking under additive measurement noise ($\sigma_{\text{noise}} = 10^{-3}$). All trajectories remain bounded and stable, with oscillations more pronounced than in the noiseless case. Across all command steps, the polynomial kernel retains the most damped and accurate response. For the first step, the unitary kernel exhibits the largest overshoot, followed by the radial basis function (RBF). In the second step, the same ranking is observed but with a reduced overshoot for the polynomial kernel. During the third and fourth steps, the RBF and unitary kernels display stronger oscillations than in the noise-free case, and the unitary shows an increased undershoot in the final stabilization phase.	70

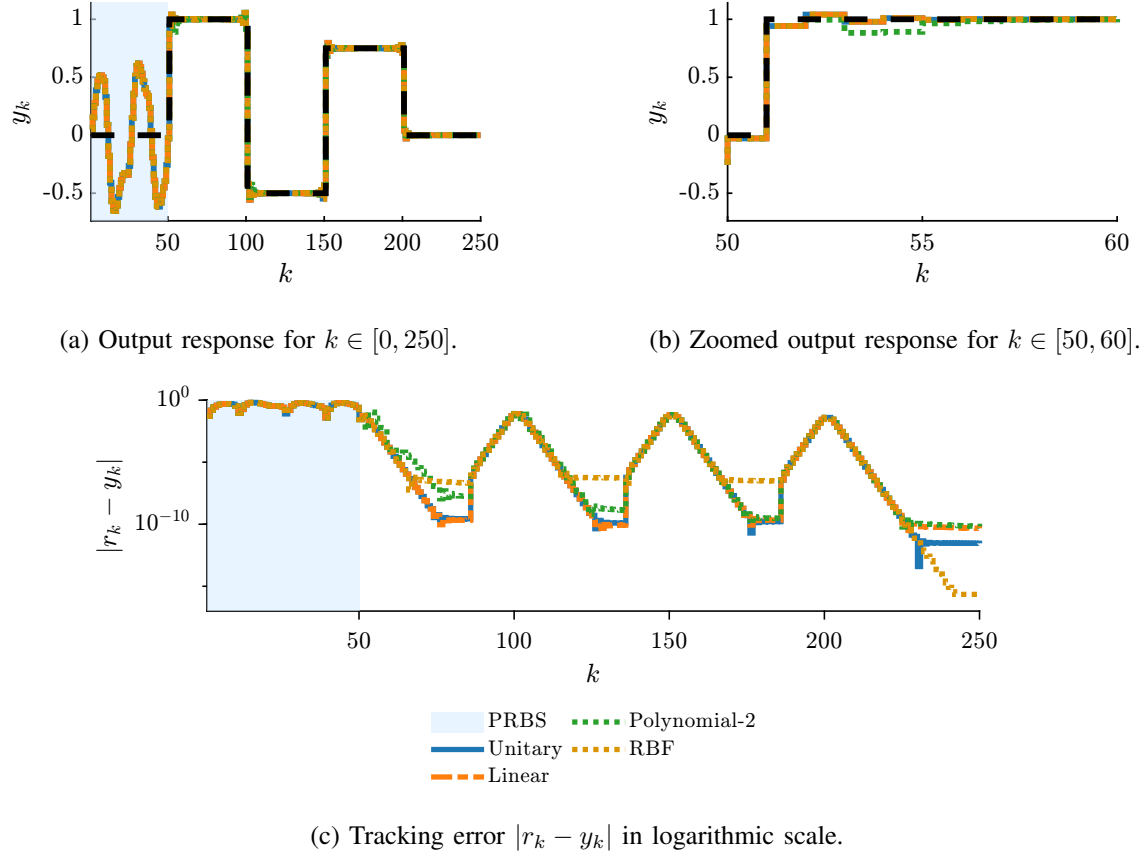


Figure 1: **Example 1.** Closed-loop output response of the four kernel configurations. Subplots (a)–(b) display the full and zoomed responses to the piecewise-constant reference signal (black dashed-line). The output trajectories for the unitary, linear, and radial-basis-function (RBF) kernels overlap, while the polynomial case initially shows a slight transient deviation for the first step command. Subplot (c) shows the absolute tracking error $|r_k - y_k|$ on a logarithmic scale. All configurations track the reference sequence with progressively smaller error. At the final command step, the steady-state errors are approximately 2.2×10^{-16} (RBF), 2.9×10^{-12} (unitary), 4.6×10^{-11} (linear), and 6.6×10^{-11} (polynomial).

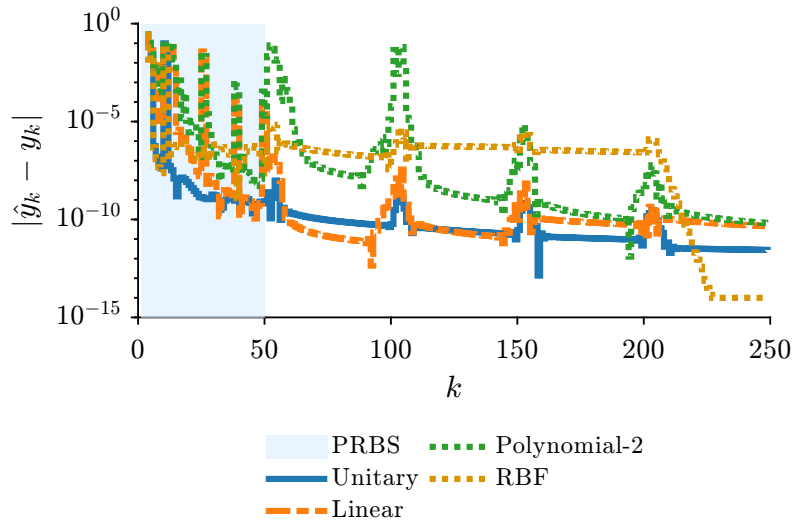


Figure 2: **Example 1.** One-step prediction error magnitude. The figure shows the instantaneous prediction error $|\hat{y}_k - y_k|$ in logarithmic scale for all kernel configurations. During the pseudo-random binary sequence (PRBS) excitation phase, all errors decrease progressively, with more pronounced transient spikes for the linear and polynomial kernels. At each command step change, short error spikes reappear for all configurations, most noticeably for the polynomial case. The radial-basis-function (RBF) kernel converges rapidly and plateaus early, remaining the least accurate overall but reaching a final prediction error of approximately 10^{-14} . The unitary kernel maintains the most consistent accuracy, with a final error of about 2.8×10^{-12} , while the linear kernel performs comparably, ending near 4.5×10^{-11} . The polynomial kernel shows larger residuals, reaching around 6.4×10^{-11} at the end of the experiment.

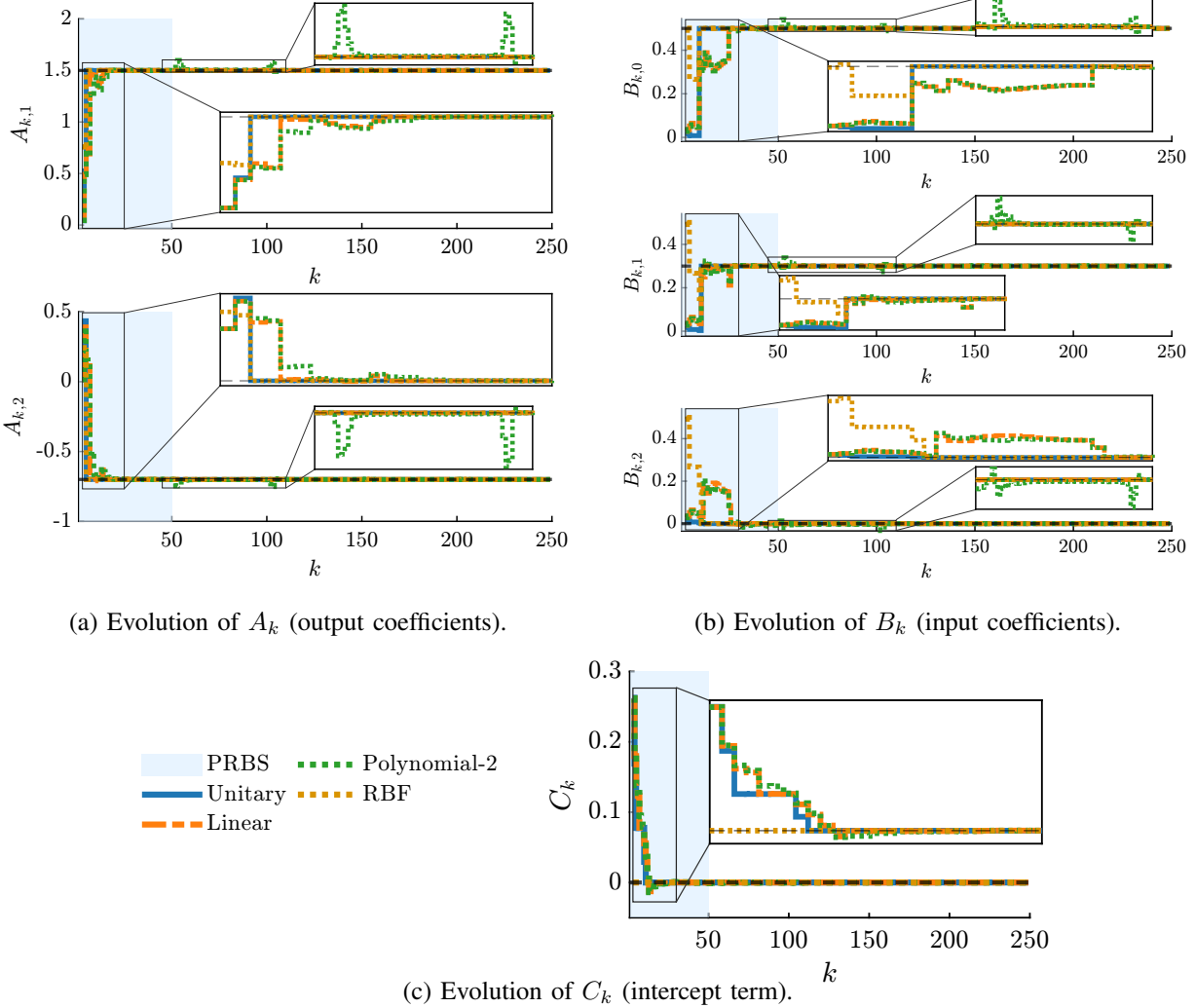
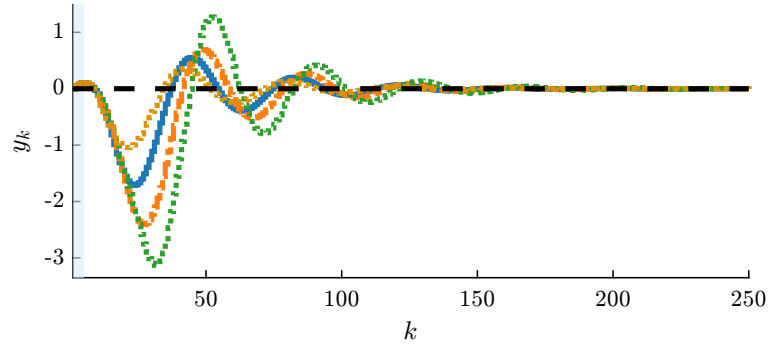
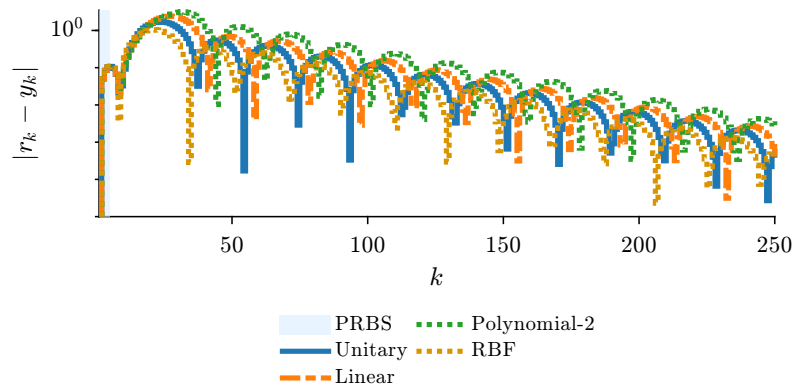


Figure 3: **Example 1.** Identified linear-parameter-varying–autoregressive-with-exogenous-input (LPV–ARX) coefficients over time. Each panel shows the estimated $A_{k,j}$, $B_{k,j}$, and C_k compared with the true parameters (dashed black). Across all kernels, the identified coefficients approach the true values after a short transient. For the A_k blocks, the unitary and radial-basis-function (RBF) kernels reach the steady level within a few steps, while the linear and polynomial kernels exhibit slower transients. When zoomed in, small fluctuations appear for the polynomial kernel around the first two command changes, indicating slightly higher sensitivity to excitation; no further variations occur afterward. A similar trend appears in B_k : both unitary and RBF responses stabilize rapidly, while the polynomial case exhibits mild fluctuations around the first two command changes. The RBF shows a slower adjustment in $B_{k,2}$ than the unitary. For the intercept C_k , all kernels evolve smoothly toward the same steady value. The RBF remains at zero throughout, while the others converge with comparable speed and without visible fluctuations.

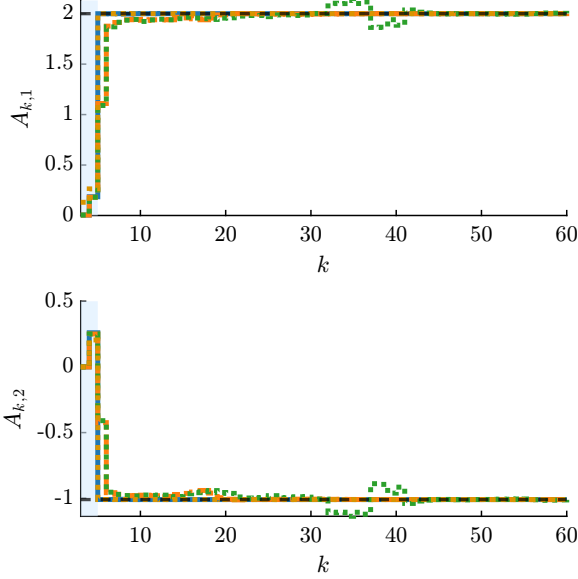


(a) Output response.

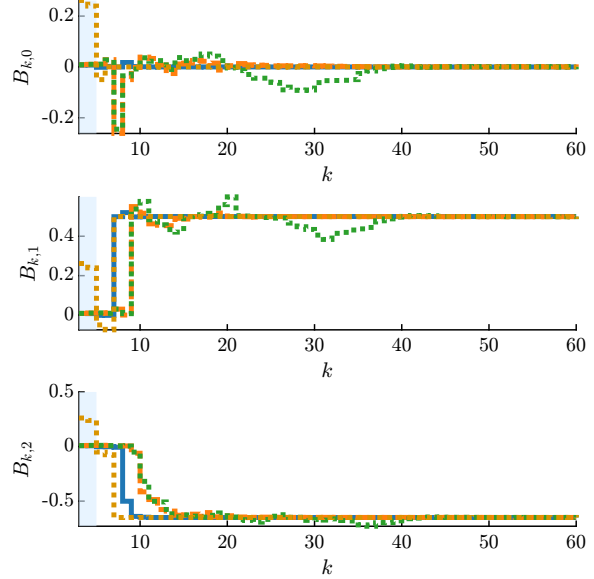


(b) Tracking error $|r_k - y_k|$ in logarithmic scale.

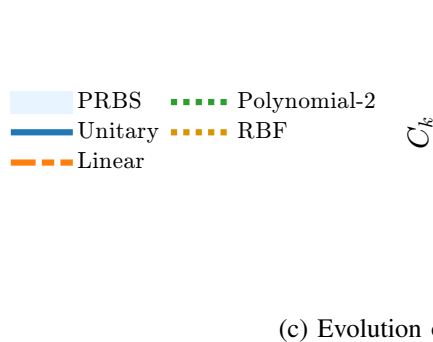
Figure 4: **Example 2a.** Closed-loop output response of the four kernel configurations. (a) All kernels start with a small overshoot followed by a negative excursion before recovering. The recovery order is radial basis function (RBF), unitary, linear, and polynomial. All responses reach stabilization, but oscillation amplitude increases in the same order, with approximate second-peak magnitudes of 0.35 (RBF), 0.54 (unitary), 0.67 (linear), and 1.26 (polynomial). The oscillation period is approximately 40 steps for all kernels. (b) Logarithmic squared-error traces with respect to the origin. Error magnitudes decrease after the PRBS phase, consistent with the attenuation of oscillations observed in (a). The same performance ranking is maintained: RBF lowest, followed by unitary, linear, and polynomial. Small envelope-like periodic modulations reflect the residual oscillatory component of the output.



(a) Evolution of A_k (output coefficients).



(b) Evolution of B_k (input coefficients).



(c) Evolution of C_k (intercept term).

Figure 5: Example 2a. Linear-parameter-varying-autoregressive-with-exogenous-input (LPV-ARX) coefficient evolution for $k \in [0, 60]$. (a) A_k : The radial-basis-function (RBF) and unitary kernels reach the true value within the pseudo-random binary sequence (PRBS) window and remain close thereafter. The linear kernel reaches the true value with moderate fluctuations and settles by about 20 steps. The polynomial kernel reaches the true value with larger fluctuations and settles by about 45 steps. Beyond 60 steps, all traces are steady; the complete history curves are omitted for clarity. (b) B_k : Similar trend. RBF and unitary settle within roughly 10 steps (about 5 steps after the 5-step PRBS). Linear settles more slowly, while polynomial shows wider fluctuations and stabilizes by about 45 steps. Beyond 60 steps all traces remain steady. (c) C_k : For the RBF kernel the intercept is already captured, yielding $C_k \equiv 0$. Unitary approaches zero within about 10 steps, linear by about 25 steps, and polynomial by about 45 steps.

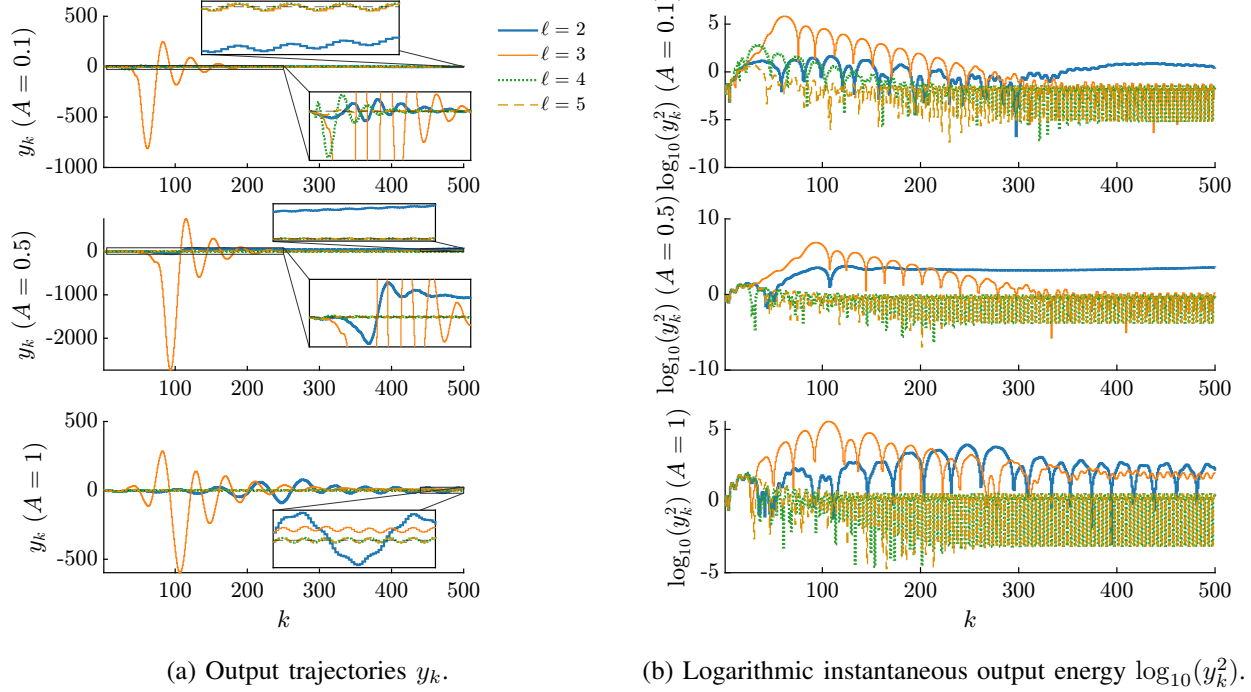
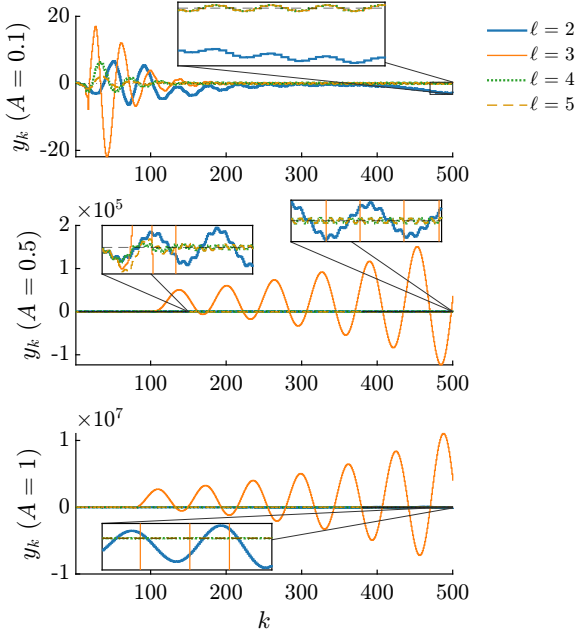
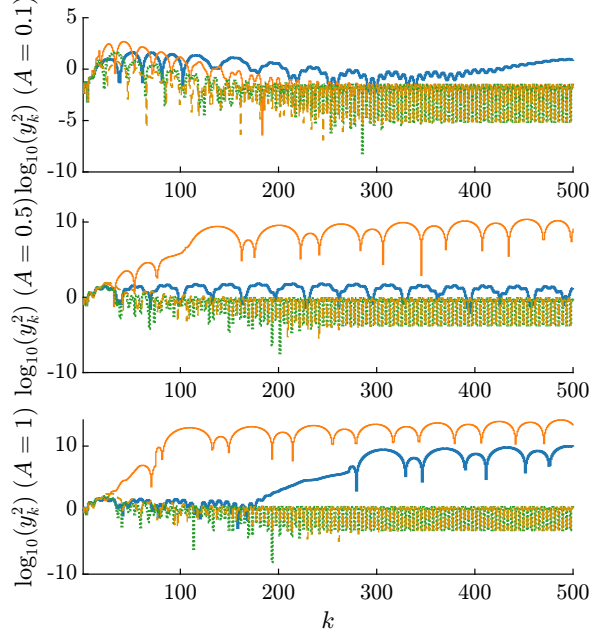


Figure 6: **Example 2b** (Unitary kernel). (a) Output responses y_k and (b) logarithmic instantaneous output energy $\log_{10}(y_k^2)$ are shown for a fixed disturbance frequency $\omega = \pi/4$. Each row corresponds to a disturbance amplitude $A \in \{0.1, 0.5, 1\}$, and, within each row, the lag order increases from $\ell = 2$ to $\ell = 5$. Across all amplitudes, the most pronounced transients occur for $\ell = 3$, lasting roughly 300 steps, as visible in both the time and logarithmic scales. Overall, $\ell = 2$ and $\ell = 3$ exhibit the largest transient amplitudes, while the smoothest and fastest settling responses are obtained for $\ell = 5$. At steady state, $\ell = 2$ consistently shows the highest residual level, remaining above all other traces from steps 350 to 500. For $A = 0.1$ and $A = 0.5$, $\ell = 3$ achieves suppression comparable to $\ell = 4$ and $\ell = 5$, whereas at $A = 1$ a small steady-state offset persists. The lowest and most stable steady-state energy levels are observed for $\ell = 4$ and $\ell = 5$, with no apparent drift over time. Linear and polynomial kernels are not shown here; their responses diverge under harmonic disturbance due to parameter chasing (see main text). These results indicate that increasing ℓ reinforces the internal-model effect in the AR structure, allowing the unitary dictionary under online RLS to capture the sinusoidal mode and achieve effective suppression at higher orders.



(a) Output trajectories y_k .



(b) Logarithmic instantaneous output energy $\log_{10}(y_k^2)$.

Figure 7: **Example 2b** (Radial-basis-function (RBF) kernel). (a) Output responses y_k and (b) logarithmic instantaneous output energy $\log_{10}(y_k^2)$ are shown for a fixed disturbance frequency $\omega = \pi/4$. Each row corresponds to a disturbance amplitude $A \in \{0.1, 0.5, 1\}$, and, within each row, the lag order increases from $\ell = 2$ to $\ell = 5$. Across all amplitudes, $\ell = 3$ consistently produces the largest transient, as visible in both the time and logarithmic scales. For $A = 0.5$ and $A = 1$, the corresponding trajectories diverge exponentially, confirmed by the sustained high levels of $\log_{10}(y_k^2)$. When $\ell = 2$, the disturbance is not effectively suppressed in any case: at $A = 0.1$ the output trajectory slowly drifts downward, at $A = 0.5$ it remains bounded but with large steady oscillations, and at $A = 1$ the amplitude grows unbounded. In contrast, for $\ell = 4$ and $\ell = 5$ the oscillations are markedly attenuated and the steady-state energy remains low and stable across all amplitudes. At $A = 0.1$, the $\ell = 2$ trace approaches a similar steady level to $\ell = 4$ and $\ell = 5$, though with a slower and less regular transient. Taken together, these results indicate that, with the RBF kernel, effective disturbance rejection emerges only for higher lag orders, typically $\ell \geq 4$, which is greater than required in the unitary case. This suggests that the RBF basis models the sinusoidal disturbance accurately once sufficient dynamic depth is provided by the autoregressive structure.

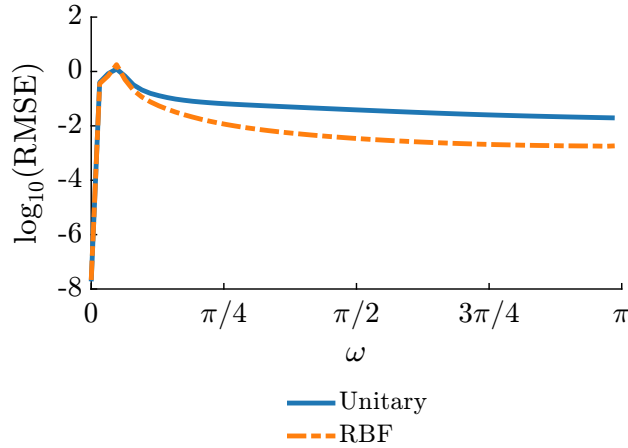
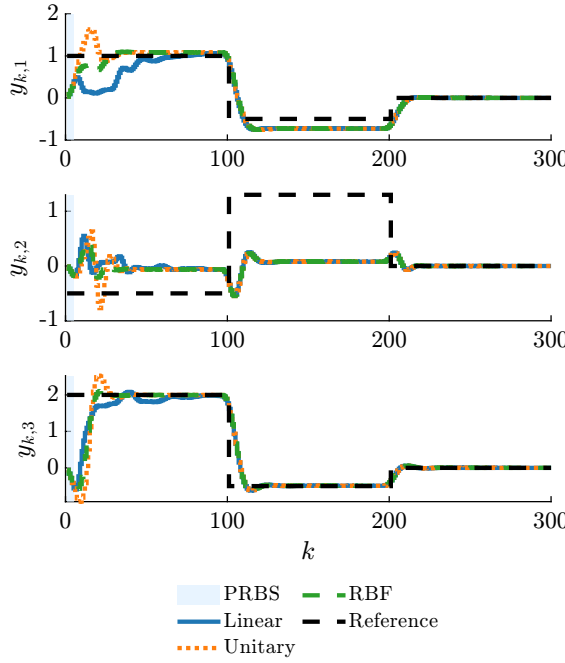
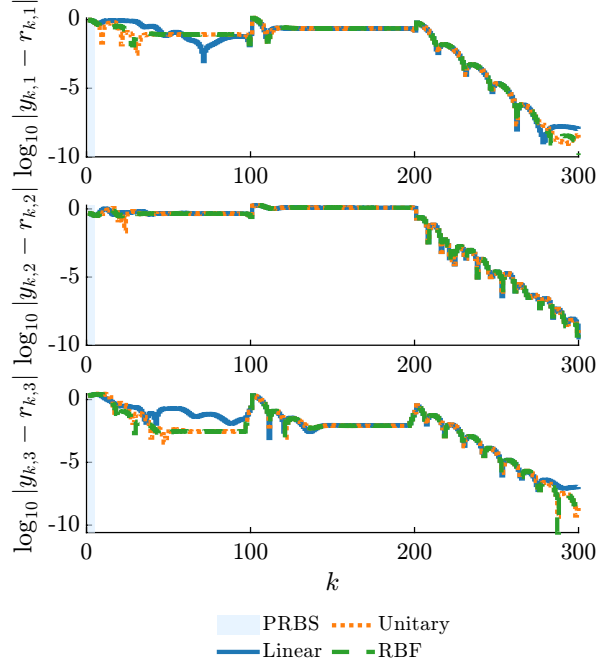


Figure 8: **Example 2b.** Frequency-domain disturbance analysis. The disturbance amplitude is fixed at $A = 0.01$ and the lag order at $\ell = 5$. For each $\omega \in [0, \pi]$, performance is evaluated over the last $T_\omega = \lceil 2\pi/\omega \rceil$ samples of a 5000-step run, while for $\omega = 0$ a fixed 1000-sample window is used. The plotted quantity is the logarithmic root-mean-square error (RMSE) evaluated over the period-aligned windows. Both kernels remain bounded over the entire frequency range and effectively reduce the disturbance energy. Their responses approximately coincide at low frequency, but diverge as ω increases, where the radial-basis-function (RBF) kernel achieves consistently lower output energy than the unitary case. See Appendix for robustness test.



(a) Output trajectories y_k .



(b) Logarithmic instantaneous error $\log_{10} |y_k - r_k|$.

Figure 9: **Example 3.** Closed-loop responses for the underactuated multi-input multi-output (MIMO) system ($m = 2$, $p = 3$) using unitary, linear, and radial-basis-function (RBF) kernels. Although the open-loop plant contains one unstable mode, all three kernels produce bounded and well-behaved closed-loop trajectories. Each output exhibits a command-tracking-like evolution rather than exact convergence, consistent with the limited steady-state reachability implied by $\text{rank } G(1) = 2 < 3$. Transient behavior differs across kernels: the linear kernel yields the slowest response, the RBF kernel responds fastest with minimal overshoot, and the unitary kernel shows the largest overshoot and undershoot before settling. Across all kernels, $y_{k,3}$ follows the reference accurately for all commands. During the first step, $y_{k,1}$ approaches its target with a small steady-state error, while $y_{k,2}$ settles around -0.06 instead of the commanded -0.5 , leaving a clear residual offset. In the second step, $y_{k,3}$ again tracks closely, whereas the first and second outputs remain bounded but retain finite tracking errors. For the final command ($r_k = 0$), all outputs decay smoothly with minimal residual error, confirming closed-loop boundedness under all kernels.

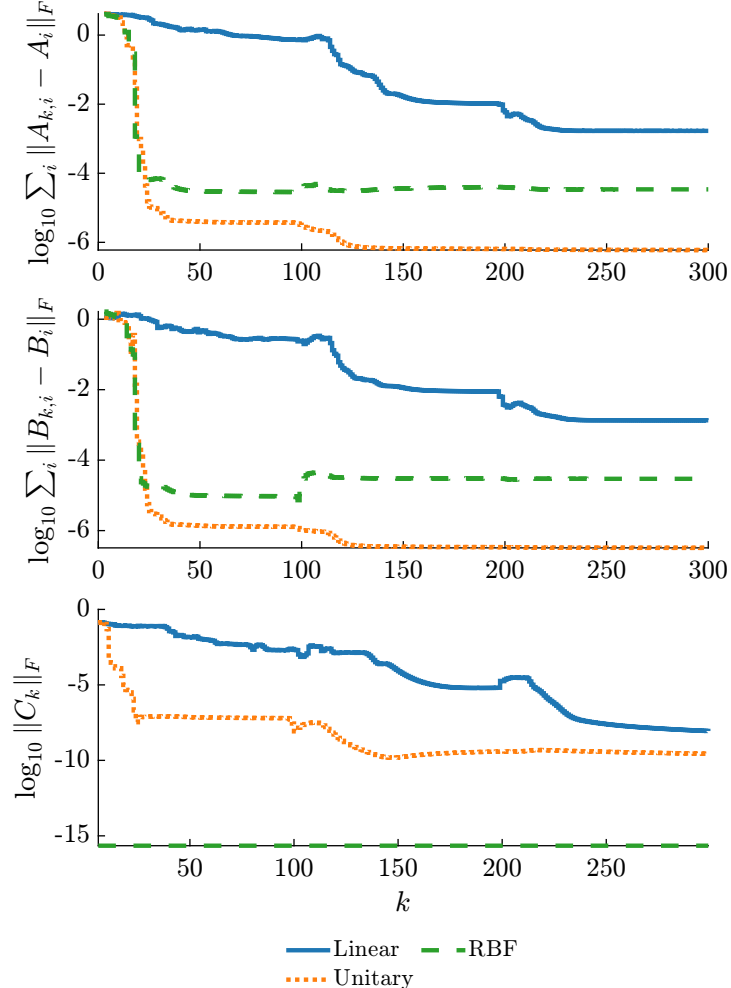


Figure 10: **Example 3:** Temporal evolution of the logarithmic identification error between the estimated and true coefficients, computed as the Frobenius norm per block and aggregated over lags. Across all kernels, the errors tend to decrease monotonically with time, with the most pronounced reduction observed for the unitary kernel. For the intercept block C_k , the radial-basis-function (RBF) kernel yields an exact match since it omits the constant feature, while the unitary kernel converges faster than the linear kernel. For the dynamic blocks A_k and B_k , the unitary kernel exhibits the fastest decay, reaching an error level around 10^{-6} , followed by the RBF (around $10^{-4.5}$) and the linear kernel (around $10^{-2.7}$).

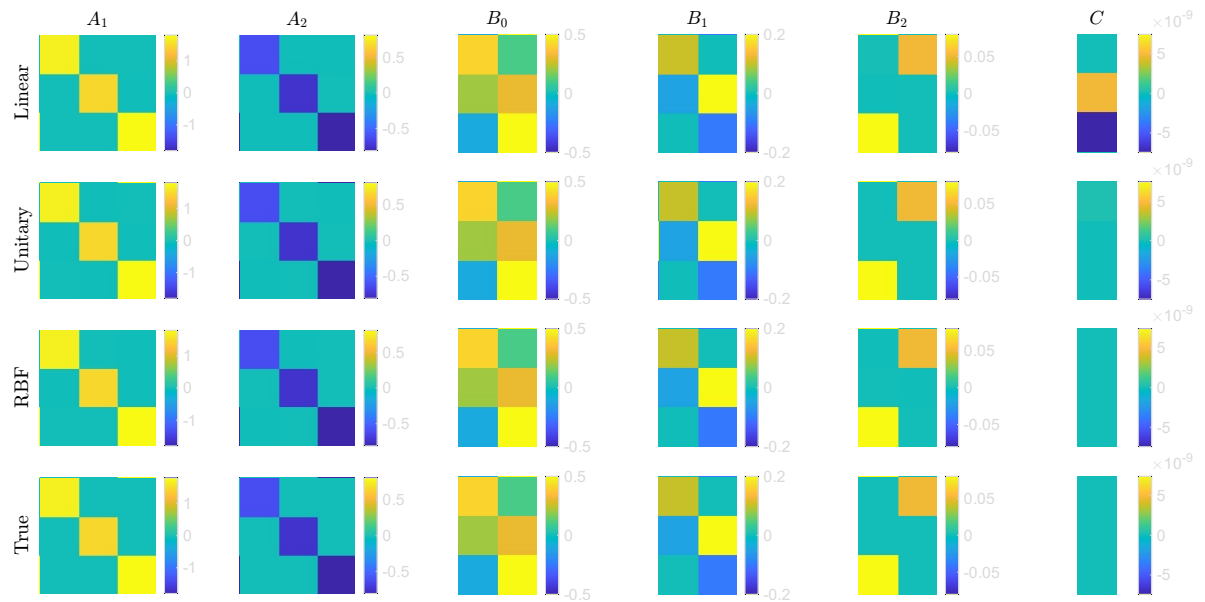
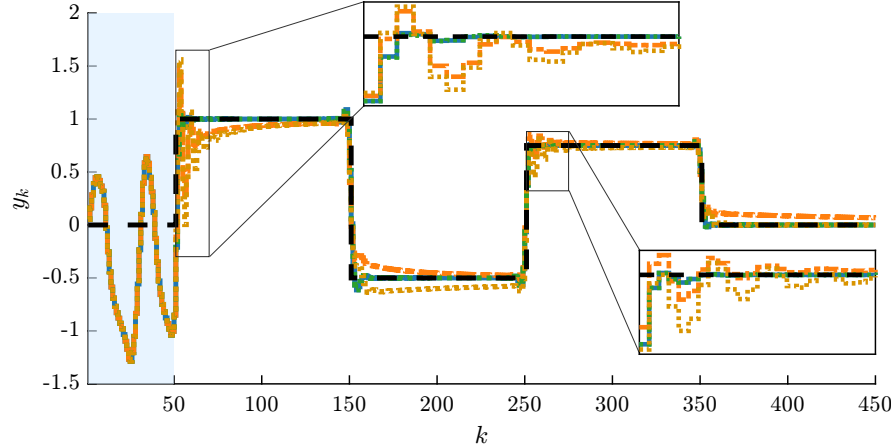
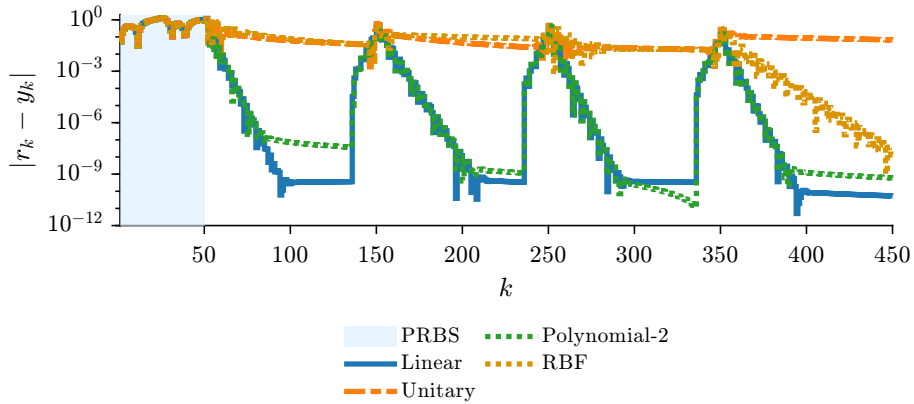


Figure 11: **Example 3.** End-of-run parameter heatmaps for A_1 , A_2 , B_0 , B_1 , B_2 , and the intercept $C \equiv 0$. Rows correspond, in order, to the linear, unitary, radial-basis-function (RBF), and true matrices. All kernels yield coefficient matrices visually close to the true ones, confirming consistent convergence of the recursive-least-squares (RLS) identification. For the intercept block C , the linear kernel produces a nearly zero matrix with residual elements on the order of 10^{-9} , while the unitary and RBF kernels remain close to or exactly zero. Overall, all identified coefficients align well with the true values, indicating accurate parameter recovery.



(a) Output trajectories y_k .



(b) Tracking error $|y_k - r_k|$ in logarithmic scale.

Figure 12: **Example 4.** Output tracking for single-input single-output (SISO) quadratic nonlinear autoregressive with exogenous input (NARX) (noncross). (a) Output y_k and command r_k (black dashed line); (b) tracking error $e_k = |y_k - r_k|$ in logarithmic scale. After the pseudo-random binary sequence (PRBS) warm-up, four step commands are applied. During the first step, the linear and polynomial kernels reach the command most rapidly, whereas the unitary and radial-basis-function (RBF) responses exhibit small oscillations and converge to values below the target. This difference is confirmed by the error trajectories: the polynomial and linear cases plateau at 3.8×10^{-8} and 3.6×10^{-10} , respectively, while the unitary and RBF saturate near 4×10^{-2} , indicating a persistent steady-state bias. A similar pattern appears in the second and third steps: in the second, the unitary kernel shows the slowest transient and the RBF maintains a larger residual error, while in the third, the polynomial kernel attains the lowest final error magnitude. In the stabilization phase ($r_k \equiv 0$), all kernels reduce the error, yet the RBF exhibits an approximately linear decay in the logarithmic scale and converges more slowly, whereas the unitary remains the least accurate ($|e_k| \approx 0.07$).

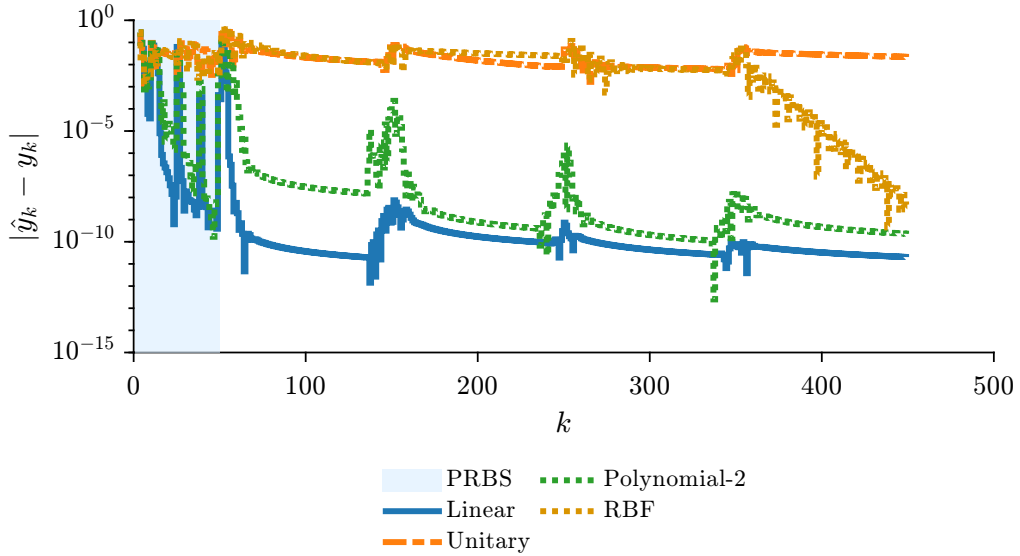
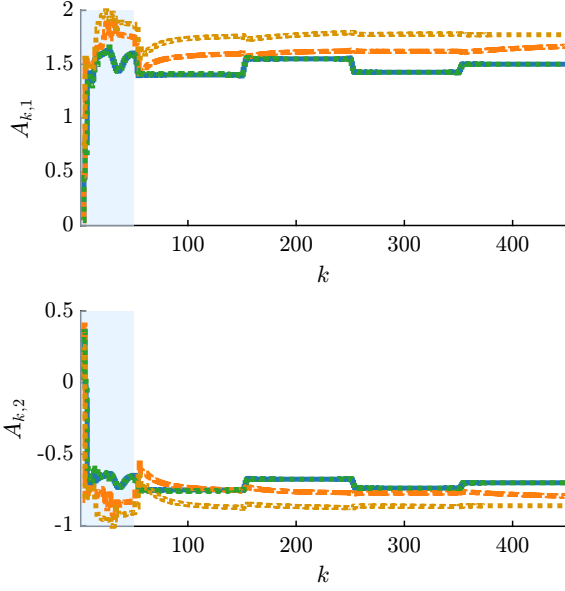
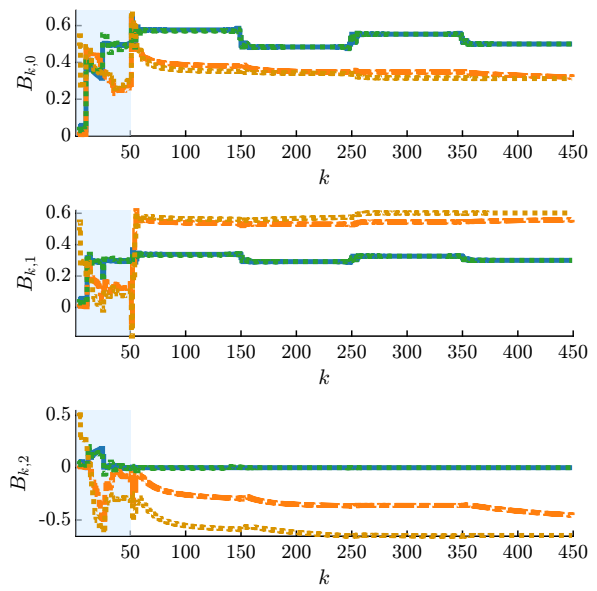


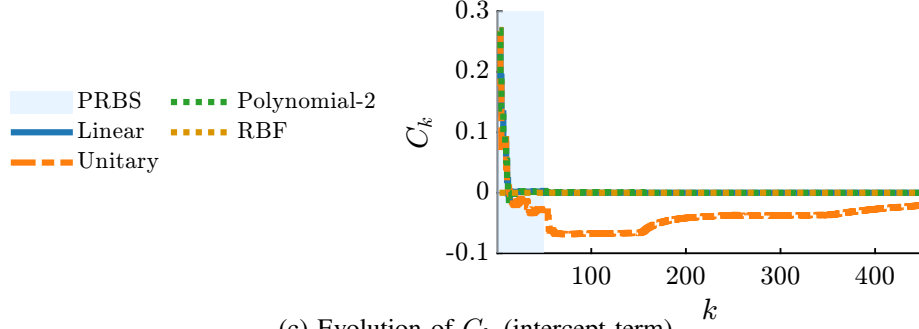
Figure 13: **Example 4.** One-step prediction error. The prediction error $|\hat{y}_k - y_k|$ is computed in a predictive framework with $\hat{y}_k = \phi_k \theta_k$, using the pre-update (*a-priori*) parameter estimate θ_k rather than the *a-posteriori* θ_{k+1} . During the pseudo-random binary sequence (PRBS) phase, the polynomial and linear kernels exhibit two pronounced transient spikes but achieve the largest overall decrease in prediction error. For each step command, the polynomial kernel shows sharper spikes yet rapidly converges, while the linear kernel attains the lowest steady values (approximately 10^{-11} with terminal plateaus near 2×10^{-11}). The polynomial follows with decreasing plateaus for successive steps, reaching about 2.3×10^{-10} . In contrast, the radial-basis-function (RBF) and unitary kernels remain less accurate, with plateau ranges between 4×10^{-3} and 2×10^{-2} across the steps. During the stabilization phase ($r_k \equiv 0$), the unitary kernel yields the poorest accuracy ($|e_k| \approx 0.022$), while the RBF error decreases nearly linearly in the logarithmic scale and gradually approaches the polynomial and linear levels.



(a) Evolution of A_k (output coefficients).

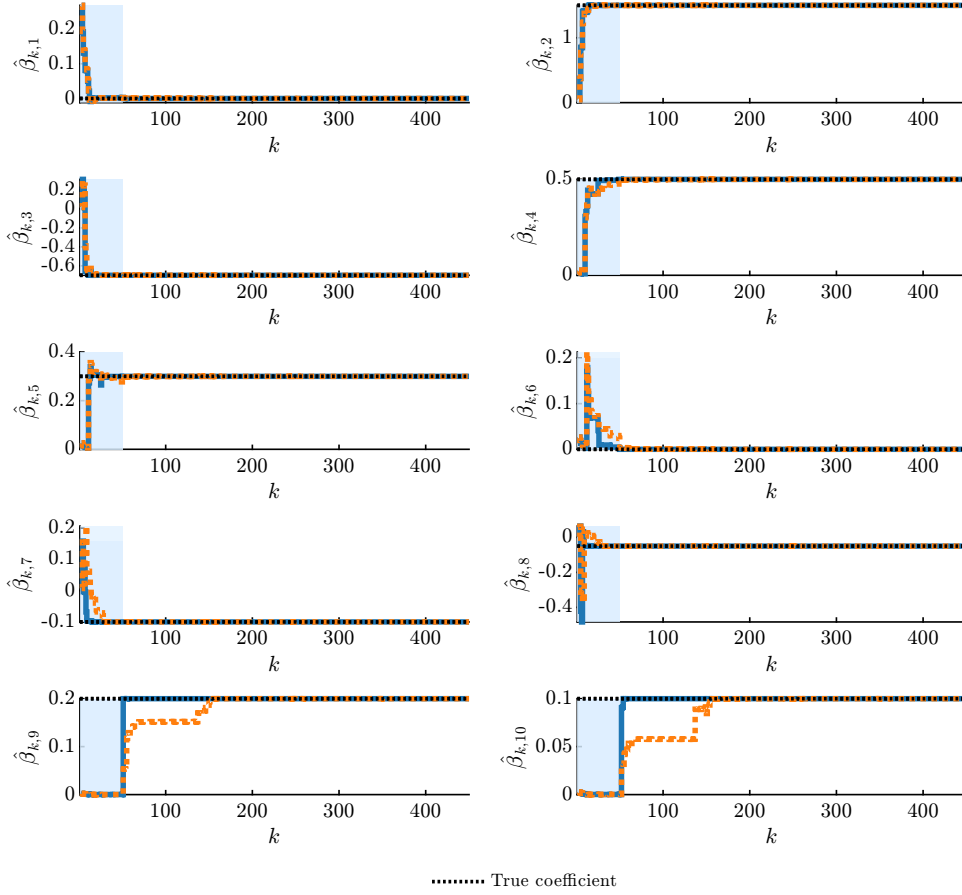


(b) Evolution of B_k (input coefficients).

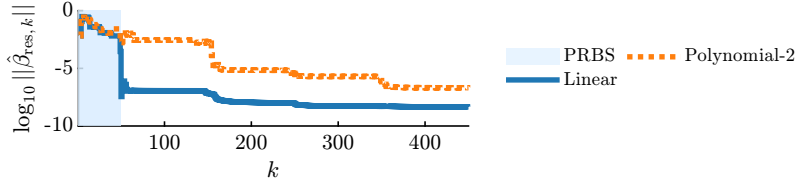


(c) Evolution of C_k (intercept term).

Figure 14: **Example 4.** Estimated linear-parameter-varying–autoregressive-with-exogenous-input (LPV–ARX) blocks $\{A_k, B_k, C_k\}$. The coefficient trajectories remain bounded with no visible drift or divergence. After each step, the linear and polynomial kernels change sharply and settle quickly, while unitary and radial basis function (RBF) evolve more slowly. The nominal linear part is $1.5 y_{k-1} - 0.7 y_{k-2} + 0.5 u_k + 0.3 u_{k-1}$. In A_k , entries $A_{k,1}$ and $A_{k,2}$ oscillate around 1.5 and -0.7 for linear/polynomial and stay in the same vicinity for unitary/RBF. This proximity likely reflects mild nonlinear effects producing small biases. In B_k , $B_{k,0}$ and $B_{k,1}$ cluster near 0.5 and 0.3 for linear/polynomial, whereas unitary/RBF deviate; the extra lag term $B_{k,2}$ is near zero only for linear/polynomial. For C_k , the linear/polynomial traces approach zero, the RBF is fixed at zero, and the unitary remains negative. During stabilization ($r_k \equiv 0$), the linear/polynomial coefficients recover the nominal linear-part values within numerical precision.

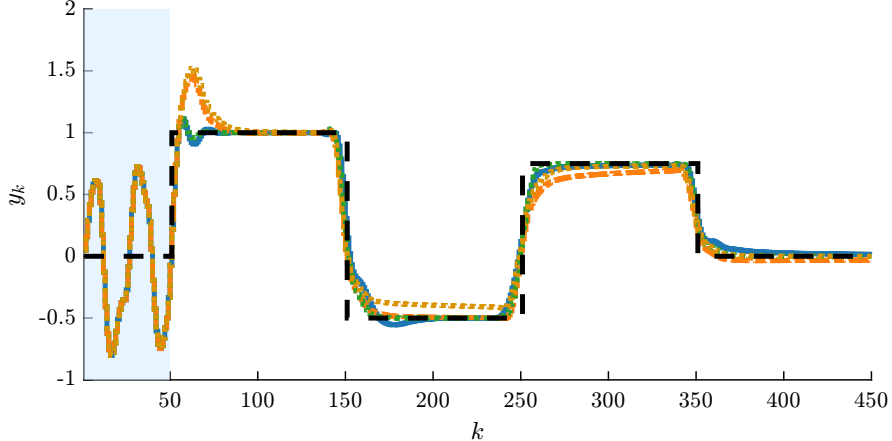


(a) Evolution of the identified coefficient vector $\hat{\beta}_k$.

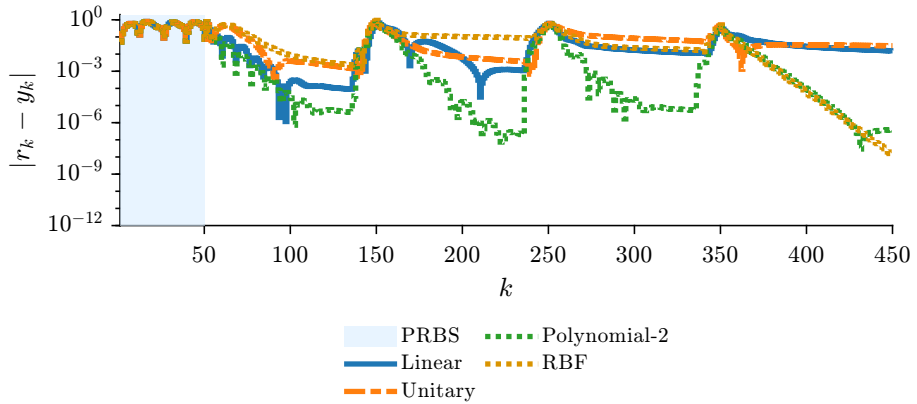


(b) Logarithmic residual norm $\log_{10} \|\hat{\beta}_{\text{res},k}\|$.

Figure 15: **Example 4.** Coefficient recovery for linear and polynomial kernels. We observe that the identified coefficients approach the true values in all cases. For components $\hat{\beta}_{k,1:8}$, most convergence occurs during the pseudo-random binary sequence (PRBS) phase. The last two components ($\hat{\beta}_{k,9:10}$) converge sharply at the onset of step commands: the linear kernel settles immediately after PRBS ($k \approx 60$), whereas the polynomial kernel converges more gradually, stabilizing near $k \approx 170$. The residual norm decreases in both cases, abruptly after the first command for the linear kernel and in a stepwise manner for the polynomial one, with the polynomial maintaining a slightly higher final residue ($\log_{10} \|\hat{\beta}_{\text{res},k}\| \approx -6.7$) than the linear kernel (≈ -8.3).



(a) Output trajectories y_k .



(b) Tracking error $|y_k - r_k|$ in logarithmic scale.

Figure 16: **Example 5.** Output tracking for the single-input single-output (SISO) cubic nonlinear autoregressive-with-exogenous-input (NARX) system with polynomial cross terms. All trajectories remain bounded and follow the command sequence with varying steady-state accuracy. During the first step, the linear and polynomial kernels yield the most damped responses, while the unitary and radial basis function (RBF) exhibit overshoots of 1.45 and 1.52, respectively. From the error plot, the polynomial achieves the lowest error (4.18×10^{-6}), followed by the linear (9.1×10^{-5}), whereas unitary and RBF remain around 3×10^{-3} . At the second step, the RBF shows the largest steady-state bias, the unitary closes the error, and the linear responds slowest; the polynomial again converges fastest with an error of about 2×10^{-7} . At the third step, the unitary performs worst, while the linear and RBF achieve similar accuracy with small residual bias; the polynomial maintains the smallest error (5.3×10^{-6}). In the final stabilization phase ($r_k \equiv 0$), unitary and linear remain least accurate, whereas RBF and polynomial decay almost linearly in the logarithmic scale; the polynomial plateaus at 3.74×10^{-7} and the RBF continues decreasing until the end of the simulation.

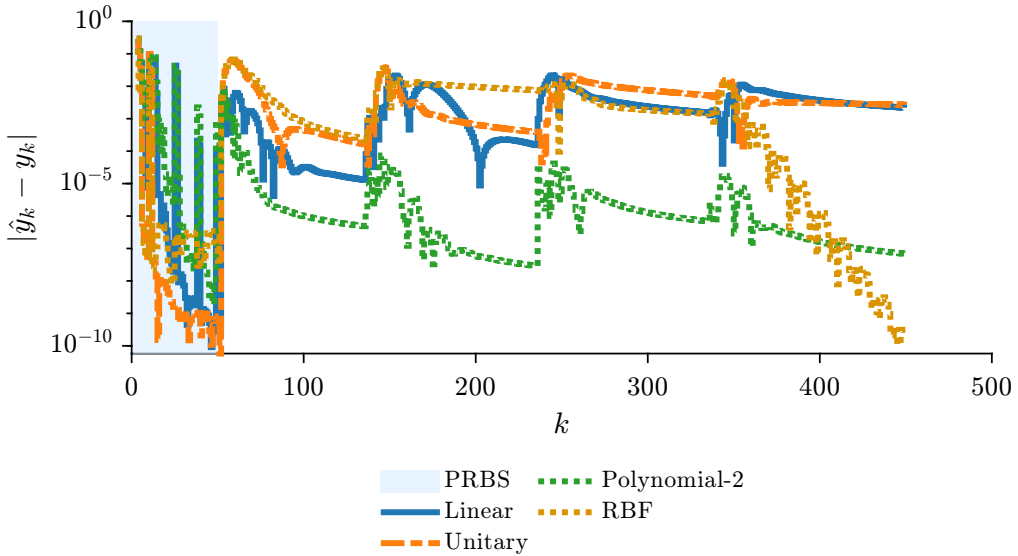
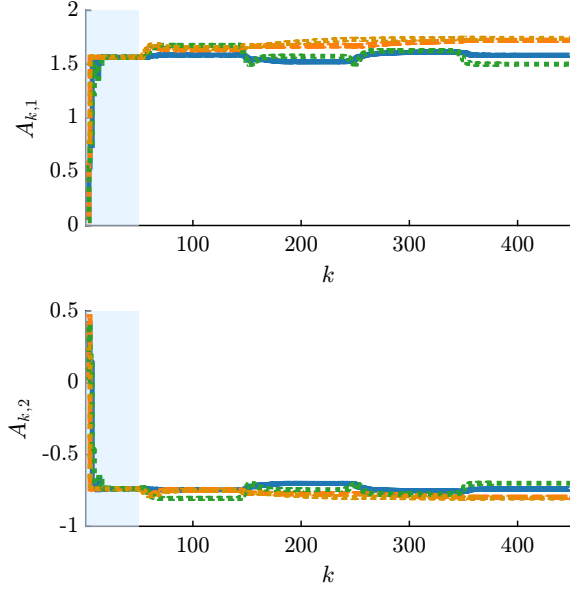
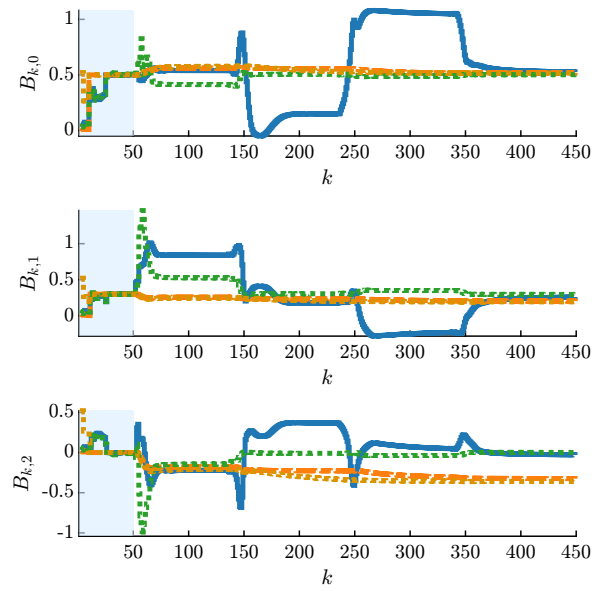


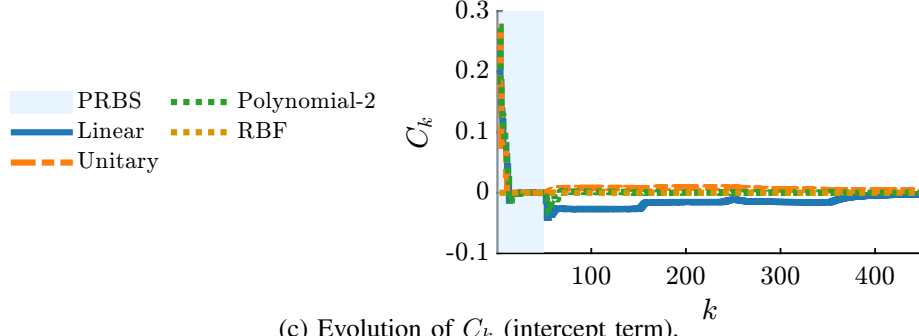
Figure 17: **Example 5.** One-step prediction error for the single-input single-output (SISO) cubic nonlinear autoregressive-with-exogenous-input (NARX) system with polynomial cross terms. During the pseudo-random binary sequence (PRBS) excitation phase, all kernels exhibit a marked reduction in prediction error; the unitary kernel attains the lowest error, followed by the linear, polynomial, and radial basis function (RBF). After the PRBS phase, a consistent ranking emerges: the polynomial kernel maintains the lowest and most stable error throughout most of the simulation, while the unitary and linear kernels show gradual degradation with each command step. For successive step commands, the unitary error plateaus at increasingly higher levels, and the linear follows a similar trend with slightly lower plateaus; by the final stabilization phase ($r_k \equiv 0$), their accuracies converge to comparable levels. The RBF kernel begins with similar accuracy to the unitary during the first step, becomes the least accurate during the second, reaches a comparable level to the linear during the third, and finally decreases linearly in the logarithmic scale to the smallest overall prediction error at the end of the simulation ($\approx 1.23 \times 10^{-10}$). This evolution coincides with the change in input excitation: during PRBS all kernels achieve low errors (unitary lowest), whereas under subsequent commanded inputs, the linear and unitary models plateau at higher error levels as their structures cannot capture the newly excited nonlinear modes; the polynomial remains consistently low, and the RBF decreases late as the trajectory revisits narrower regions of the input–output space.



(a) Evolution of A_k (output coefficients).

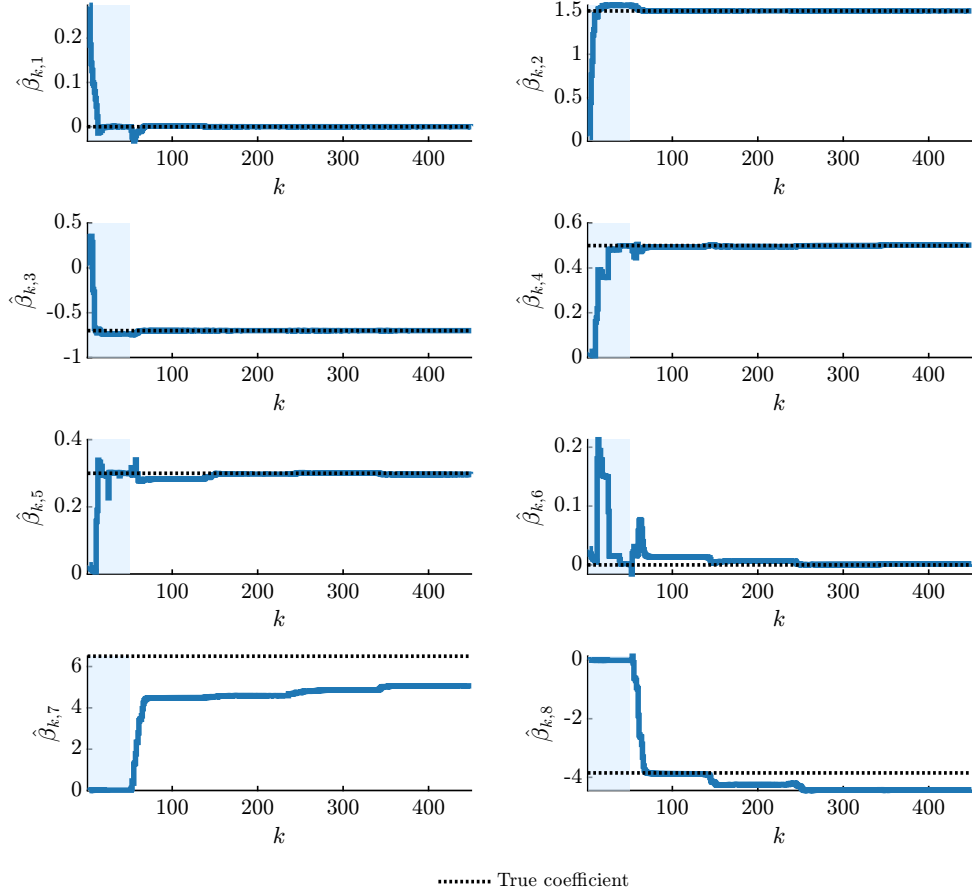


(b) Evolution of B_k (input coefficients).

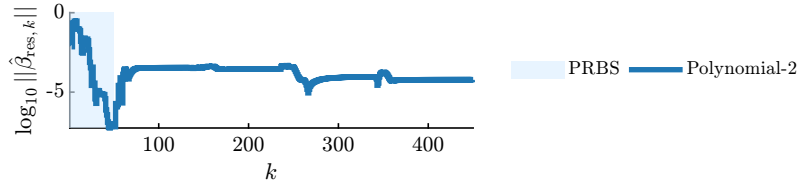


(c) Evolution of C_k (intercept term).

Figure 18: **Example 5.** Linear-parameter-varying–autoregressive-with-exogenous-input (LPV–ARX) coefficient evolution. All estimated coefficients remain bounded and respond to command changes. For $A_{k,1}$, the linear and polynomial kernels stay closest to the nominal linear coefficient 1.5 (the true value associated with y_{k-1} in the linear backbone of the cubic nonlinear autoregressive-with-exogenous-input (NARX) model), whereas the unitary and radial basis function (RBF) deviate more. For $A_{k,2}$, all trajectories oscillate around the nominal value -0.7 , corresponding to the coefficient of y_{k-2} in the same linear backbone. The B_k coefficients remain bounded, with the largest variations observed for the linear and polynomial cases. All C_k terms stay near zero, the linear kernel showing the largest offset. These bounded oscillations and coefficient shifts are consistent with the excitation of nonlinear components and structure-dependent sensitivity.

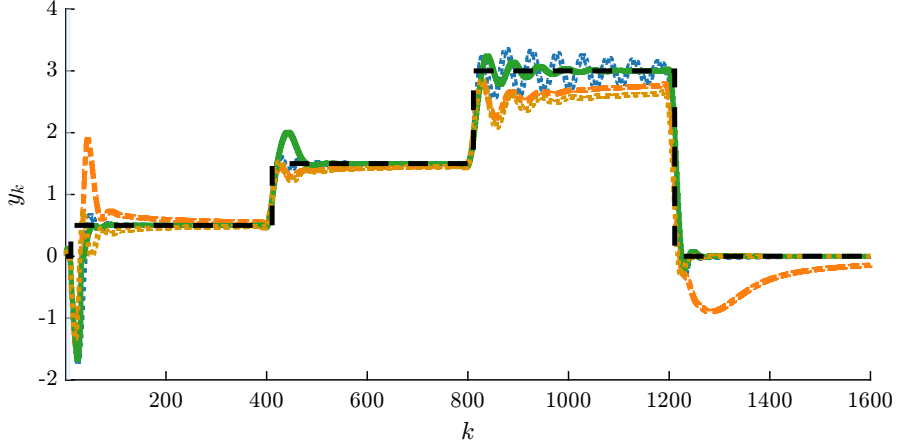


(a) Evolution of the identified coefficient vector $\hat{\beta}_k$.

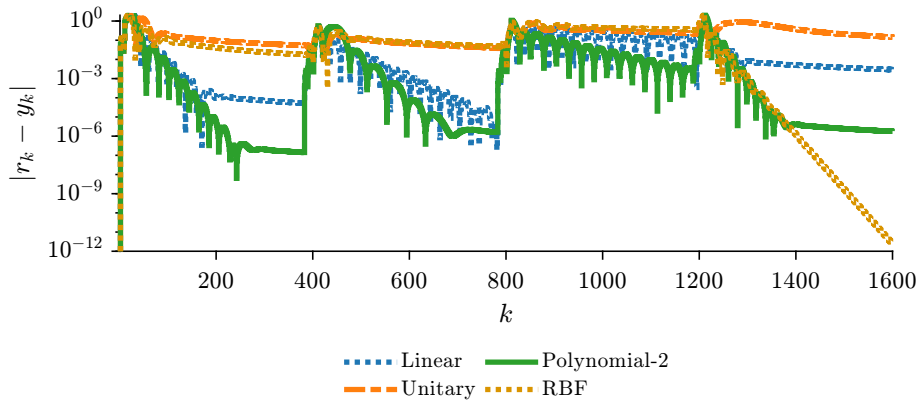


(b) Logarithmic residual norm $\log_{10} \|\hat{\beta}_{\text{res},k}\|$.

Figure 19: **Example 5** (Polynomial case only). Identified parameters at indices aligned with the true parameterization. During pseudo-random binary sequence (PRBS), the linear-part coefficients $\hat{\beta}_{k,1:6}$ move toward their true values and remain close thereafter. In the control phase, the cross coefficients evolve: $\hat{\beta}_{k,7}$ rises toward 6.5 but ends at 5.06; $\hat{\beta}_{k,8}$ drops near -3.85 early, then overshoots and ends at -4.43 . The residual decreases markedly during PRBS, increases around the first step, decreases again around the third step, and settles near -4.2 (log scale) by the end. Note that the near-zero values of $\hat{\beta}_{k,7:8}$ during PRBS are consistent with limited excitation of the cubic cross features.



(a) Output trajectories y_k .



(b) Tracking error $|y_k - r_k|$ in logarithmic scale.

Figure 20: **Example 6.** Output tracking and logarithmic error. All kernels remain bounded throughout the simulation. For the first step ($r_k = 0.5$), the unitary kernel exhibits the largest overshoot and slowest convergence, followed by the radial basis function (RBF) with a milder transient. The linear and polynomial kernels show smaller overshoots, with residual errors of 5.2×10^{-5} and 1.47×10^{-7} , respectively, while the unitary and RBF settle around 0.06 and 0.02. As the command increases to $r_k = 1.5$, the nonlinear influence strengthens: the polynomial overshoots most but, with the linear kernel, achieves the smallest steady-state error; RBF and unitary remain less accurate. At $r_k = 3$, the nonlinear distortion dominates; the linear kernel oscillates and gradually damps, while the polynomial tracks more closely despite mild oscillations. RBF and linear exhibit the largest deviations (≈ 0.3). In the final stabilization phase ($r_k \equiv 0$), all trajectories stay bounded; the unitary shows a persistent undershoot, and both polynomial and RBF display monotonic error decay, the RBF ending with the smallest final error by the end of the simulation.

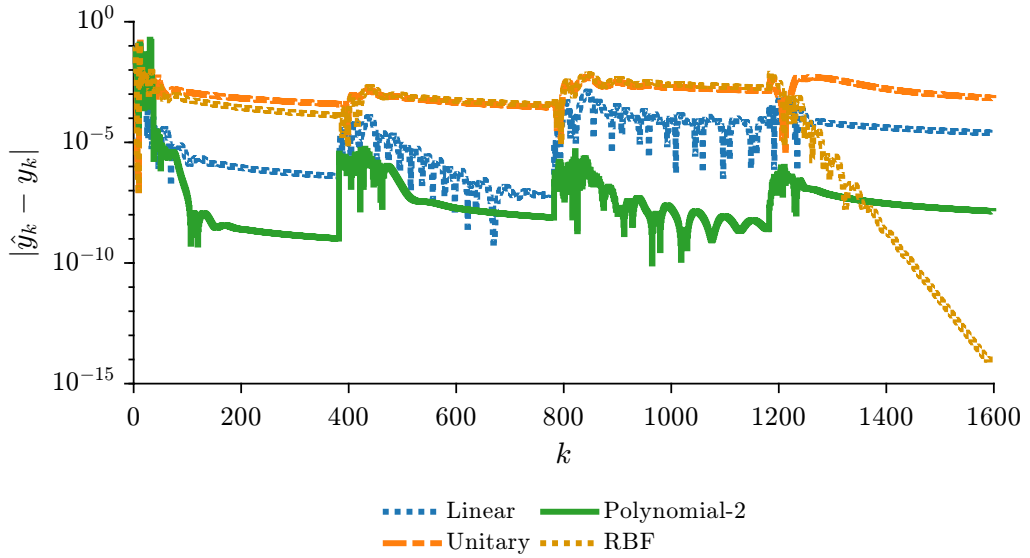


Figure 21: **Example 6.** One-step prediction error in logarithmic scale. For the first three command steps, the unitary and radial-basis-function (RBF) kernels yield the poorest prediction accuracy, their traces remaining close throughout. They are followed by the linear kernel, while the polynomial consistently attains the lowest errors across all steps, reflecting its ability to represent the cubic input nonlinearity more accurately. During the final stabilization phase, the unitary kernel still plateaus at a high level, whereas the RBF error decays linearly and ends as the smallest among all kernels.

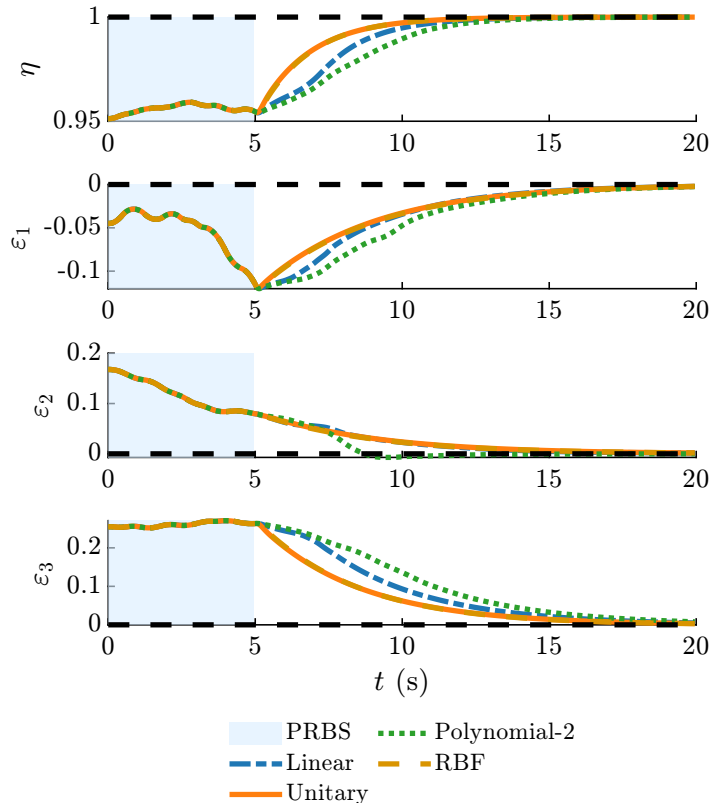


Figure 22: **Example 7:** Closed-loop quaternion trajectories with a fixed desired attitude $q_d = [1 \ 0 \ 0 \ 0]^\top$. The unitary and radial-basis-function (RBF) kernels exhibit a first-order-like transient response characterized by a nonzero initial slope followed by exponential-type convergence toward the commanded equilibrium. Across all quaternion components, the unitary and RBF responses nearly coincide throughout both transient and steady-state phases, indicating that the two parameterizations capture the local attitude dynamics equivalently. The polynomial kernel displays a slightly faster settling in ε_2 , whereas for the remaining components the polynomial and linear kernels converge more slowly.

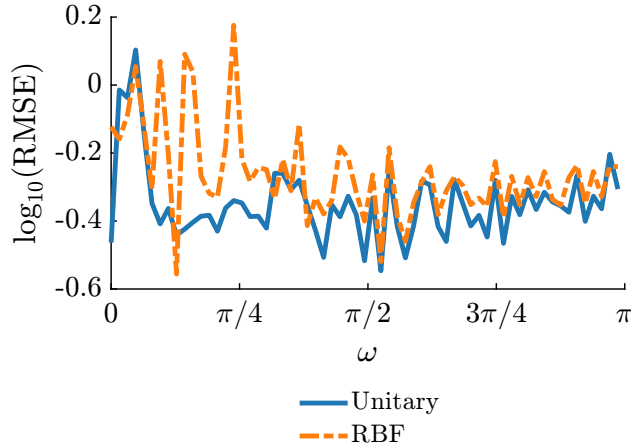


Figure 23: **Example 2b** (Robustness test). Frequency-domain disturbance test repeated under additive Gaussian noise with standard deviation $\sigma_{\text{noise}} = 10^{-2}$. All other parameters are identical to the noiseless case ($A = 0.01$, $\ell = 5$, and $\omega \in [0, \pi]$ with step 0.05). The plotted quantity is the logarithmic root-mean-square error (RMSE) of the noise-free output y_k evaluated over the period-aligned windows. Both kernels remain bounded across all frequencies and preserve the qualitative attenuation pattern observed in the noiseless experiment. Their curves now lie close to each other, with the radial-basis-function (RBF) trace slightly above the unitary over most of the band, indicating comparable but marginally weaker suppression in the presence of noise.

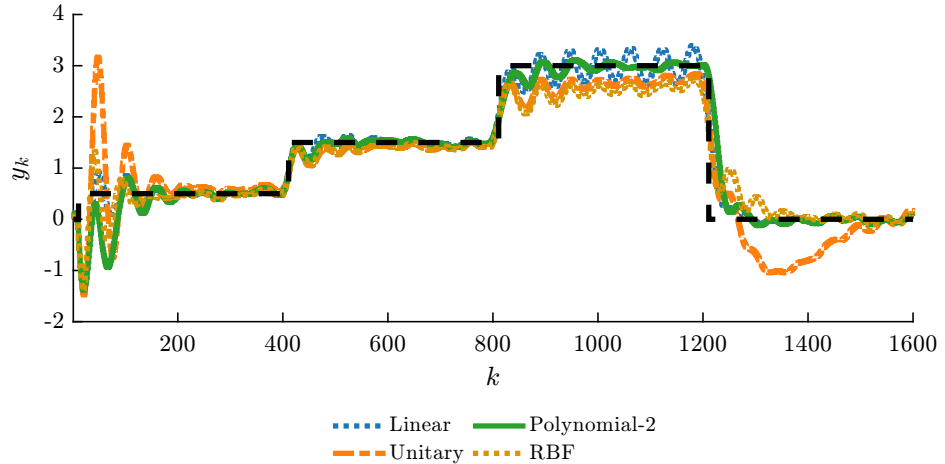


Figure 24: **Example 6** (Robustness test). Output tracking under additive measurement noise ($\sigma_{\text{noise}} = 10^{-3}$). All trajectories remain bounded and stable, with oscillations more pronounced than in the noiseless case. Across all command steps, the polynomial kernel retains the most damped and accurate response. For the first step, the unitary kernel exhibits the largest overshoot, followed by the radial basis function (RBF). In the second step, the same ranking is observed but with a reduced overshoot for the polynomial kernel. During the third and fourth steps, the RBF and unitary kernels display stronger oscillations than in the noise-free case, and the unitary shows an increased undershoot in the final stabilization phase.

List of Tables

2	Example 1: Performance metrics. Root-mean-square error (RMSE) and integral absolute error (IAE) quantify output tracking accuracy; total variation of the input (TV_u) and peak input amplitude ($Peak_u$) characterize input activity. All kernel configurations exhibit nearly identical closed-loop performance, with RMSE ≈ 0.017 , IAE ≈ 0.93 , and comparable total variation of the input ($TV_u \approx 46.4$) and peak input amplitude ($Peak_u \approx 2.6$). The polynomial kernel shows slightly elevated tracking error and input activity, while the unitary, linear, and radial-basis-function (RBF) kernels remain indistinguishable within numerical precision. These results confirm consistent controller behavior across kernel types in this linear scenario.	74
2	Example 2a: Performance metrics. In bold: kernel with the lowest root-mean-square error (RMSE) and integral absolute error (IAE). The radial-basis-function (RBF) kernel produces the smallest tracking error and control effort, reflected in its minimal RMSE, IAE, and total variation of the input (TV_u) values. The unitary kernel performs similarly, maintaining stable dynamics with moderate input usage. Linear and polynomial kernels show larger steady-state oscillations and increased integrated error, with the polynomial case also exhibiting the greatest control variability and peak magnitude. These numerical outcomes align with the transient behavior illustrated in Figures 4 and 5.	75
20	Example 2b: Performance metrics for $\omega = \pi/4$. Disturbance amplitudes $A \in \{0.1, 0.5, 1\}$ and lag orders $\ell \in \{2, 3, 4, 5\}$. Bold row: lag ℓ for a fixed A yielding the lowest root-mean-square error (RMSE) and integral absolute error (IAE); red row: diverging cases. For the unitary kernel, all runs remain bounded, though large transients occur for $\ell = 3$, where both RMSE and IAE rise by more than two orders of magnitude relative to other settings. At each amplitude, performance improves monotonically with lag order: $\ell = 2$ yields the largest steady-state error, whereas $\ell = 4$ and $\ell = 5$ reach the lowest RMSE and IAE with moderate control effort. For example, at $A = 1$, the metrics drop from RMSE = 27.26 at $\ell = 2$ to roughly 1.9 at $\ell = 4$ and $\ell = 5$, accompanied by a marked reduction in total variation of the input (TV_u). This aligns with the visual evidence of smoother, more stable trajectories for higher ℓ . For the radial-basis-function (RBF) kernel, instability emerges for $\ell = 3$ at moderate and large amplitudes, where the errors grow exponentially. At $\ell = 2$, the responses remain bounded but exhibit significant drift or persistent residual oscillations. Only for $\ell \geq 4$ does the closed loop stabilize, yielding small RMSE and IAE with limited control activity. The improvement from $\ell = 3$ to $\ell = 4$ is substantial; increasing the lag order restores disturbance rejection across all amplitudes. These findings indicate that both kernels benefit from longer regressors, but the RBF kernel requires greater lag depth to attain robustness comparable to the unitary case. The numerical metrics are consistent with the qualitative behavior seen in the output/log-energy plots.	76

Example 3: Control-effort metrics. Total variation of the input (TV_u) and peak input magnitude (Peak_u). Higher TV_u indicates stronger actuation. The radial-basis-function (RBF) kernel yields the smoothest input, followed by the linear and unitary cases. The results show that the unitary kernel yields the largest overall actuation and highest peak input, matching its stronger overshoot seen in the output trajectories. The linear kernel exhibits slightly reduced total variation, while the RBF kernel provides the smoothest control action, giving the smallest TV_u and the lowest peak amplitude. These numerical values are consistent with the transient behavior in Figure 9, where the RBF response is fastest and least oscillatory.

77

Example 4: Performance metrics. Root-mean-square error (RMSE) and integral absolute error (IAE) quantify output tracking accuracy; total variation of the input (TV_u) and peak input magnitude ($Peak_u$) characterize input activity. Linear and polynomial kernels produce the lowest tracking errors and similar input activity, indicating nearly identical behavior. Unitary and radial-basis-function (RBF) kernels exhibit higher RMSE and IAE, along with increased input variation and larger control peaks. All methods remain stable and bounded, consistent with the parameter evolution shown in Figures 14 and 15.

78

Example 5: Performance metrics. Root-mean-square error (RMSE) and integral absolute error (IAE) quantify output tracking accuracy; total variation of the input (TV_u) and peak input magnitude ($Peak_u$) characterize control activity. The polynomial kernel attains the smallest tracking error in both RMSE and IAE, reflecting its direct representation of the cubic cross terms. The linear kernel delivers intermediate accuracy, whereas the unitary and radial-basis-function (RBF) kernels show the largest residuals, consistent with their observable steady-state biases. All methods exhibit similar control activity, with TV_u and $Peak_u$ confined to a narrow range, indicating that the polynomial kernel's higher accuracy is not achieved through increased control effort. These findings support the conclusion that explicit polynomial features provide the most balanced performance in this nonlinear setting.

79

Example 6: Performance metrics. Root-mean-square error (RMSE) and integral absolute error (IAE) quantify output tracking accuracy; total variation of the input (TV_u) and peak input magnitude ($Peak_u$) characterize control activity. The polynomial kernel achieves the smallest RMSE and IAE, consistent with its accurate representation of the cubic input nonlinearity. The linear kernel provides intermediate accuracy, whereas the unitary and RBF kernels produce larger tracking errors and greater accumulated deviations. Among these, the unitary kernel yields the highest IAE, matching its visible undershoot and slower convergence. Control activity measures, including TV_u and $Peak_u$, remain similar across all kernels, indicating that the polynomial kernel's improved accuracy does not rely on elevated input effort. These numerical outcomes reinforce the ranking implied by the plots.

80

Example 7: Performance metrics for attitude stabilization. Lower values of root-mean-square error (RMSE) and integral absolute error (IAE) indicate higher tracking accuracy; total variation of the input (TV_u) and peak input magnitude ($Peak_u$) quantify control activity. Although the linear and polynomial kernels appear to converge more slowly in the time-domain plots (see Figure 22), their steady-state tracking accuracy, which is measured by RMSE and IAE, is superior. This follows from the fact that the performance metric includes the angular-velocity components of the output vector, and the linear and polynomial kernels produce smoother responses with reduced velocity amplitudes. As a result, their trajectories remain closer to the reference, which is zero for both attitude and angular rate, despite slower transient convergence. The unitary and radial-basis-function (RBF) kernels reach equilibrium more rapidly but with slightly larger velocity excursions, leading to higher accumulated error. Control activity is similar across all methods, indicating that the accuracy differences stem from the trade-off between transient speed and overall output smoothness rather than variations in control effort.

81

Example 6 (Appendix): Performance metrics under additive measurement noise stress. Root-mean-square error (RMSE) and integral absolute error (IAE) quantify output tracking accuracy; total variation of the input (TV_u) and peak input magnitude ($Peak_u$) characterize control activity. The ranking of the kernels remains consistent with the noiseless case: the polynomial kernel attains the lowest RMSE and IAE, followed by the linear kernel, while the unitary and radial-basis-function (RBF) kernels display larger tracking errors. The uniform increase in all error metrics reflects the influence of measurement noise, yet all trajectories stay bounded and stable. Control activity measures (TV_u , $Peak_u$) remain similar across kernels, indicating that the polynomial kernel preserves its accuracy without additional input effort. These numerical results align with the trends visible in Figure 24.

82

TABLE 1: **Example 1:** Performance metrics. Root-mean-square error (RMSE) and integral absolute error (IAE) quantify output tracking accuracy; total variation of the input (TV_u) and peak input amplitude ($Peak_u$) characterize input activity. All kernel configurations exhibit nearly identical closed-loop performance, with $RMSE \approx 0.017$, $IAE \approx 0.93$, and comparable total variation of the input ($TV_u \approx 46.4$) and peak input amplitude ($Peak_u \approx 2.6$). The polynomial kernel shows slightly elevated tracking error and input activity, while the unitary, linear, and radial-basis-function (RBF) kernels remain indistinguishable within numerical precision. These results confirm consistent controller behavior across kernel types in this linear scenario.

Kernel	RMSE	IAE	TV_u	$Peak_u$
Unitary	0.0172	0.928	46.40	2.60
Linear	0.0172	0.928	46.40	2.60
RBF	0.0172	0.928	46.40	2.60
Polynomial-2	0.0221	1.186	48.49	2.61

TABLE 2: **Example 2a:** Performance metrics. In bold: kernel with the lowest root-mean-square error (RMSE) and integral absolute error (IAE). The radial-basis-function (RBF) kernel produces the smallest tracking error and control effort, reflected in its minimal RMSE, IAE, and total variation of the input (TV_u) values. The unitary kernel performs similarly, maintaining stable dynamics with moderate input usage. Linear and polynomial kernels show larger steady-state oscillations and increased integrated error, with the polynomial case also exhibiting the greatest control variability and peak magnitude. These numerical outcomes align with the transient behavior illustrated in Figures 4 and 5.

Kernel	RMSE	IAE	TV_u	$Peak_u$
RBF	0.2470	26.98	0.451	0.100
Unitary	0.4076	44.42	0.721	0.135
Linear	0.5901	64.56	0.823	0.134
Polynomial-2	0.8059	95.39	1.374	0.188

TABLE 3: **Example 2b:** Performance metrics for $\omega = \pi/4$. Disturbance amplitudes $A \in \{0.1, 0.5, 1\}$ and lag orders $\ell \in \{2, 3, 4, 5\}$. Bold row: lag ℓ for a fixed A yielding the lowest root-mean-square error (RMSE) and integral absolute error (IAE); red row: diverging cases. For the unitary kernel, all runs remain bounded, though large transients occur for $\ell = 3$, where both RMSE and IAE rise by more than two orders of magnitude relative to other settings. At each amplitude, performance improves monotonically with lag order: $\ell = 2$ yields the largest steady-state error, whereas $\ell = 4$ and $\ell = 5$ reach the lowest RMSE and IAE with moderate control effort. For example, at $A = 1$, the metrics drop from RMSE = 27.26 at $\ell = 2$ to roughly 1.9 at $\ell = 4$ and $\ell = 5$, accompanied by a marked reduction in total variation of the input (TV_u). This aligns with the visual evidence of smoother, more stable trajectories for higher ℓ . For the radial-basis-function (RBF) kernel, instability emerges for $\ell = 3$ at moderate and large amplitudes, where the errors grow exponentially. At $\ell = 2$, the responses remain bounded but exhibit significant drift or persistent residual oscillations. Only for $\ell \geq 4$ does the closed loop stabilize, yielding small RMSE and IAE with limited control activity. The improvement from $\ell = 3$ to $\ell = 4$ is substantial; increasing the lag order restores disturbance rejection across all amplitudes. These findings indicate that both kernels benefit from longer regressors, but the RBF kernel requires greater lag depth to attain robustness comparable to the unitary case. The numerical metrics are consistent with the qualitative behavior seen in the output/log-energy plots.

Kernel	(A, ℓ)	RMSE	IAE	TV_u	$Peak_u$
Unitary	(0.1,2)	2.15	841.6	9.46	0.69
	(0.1,3)	138.95	22081.2	388.20	71.36
	(0.1,4)	4.21	712.3	27.51	5.25
	(0.1,5)	0.41	103.7	1.06	0.16
	(0.5,2)	44.32	20290.9	25.88	4.88
	(0.5,3)	465.31	75191.2	1224.65	184.55
	(0.5,4)	0.98	342.8	3.23	0.37
	(0.5,5)	1.11	365.3	2.57	0.38
	(1,2)	27.26	9557.5	65.17	3.83
	(1,3)	119.68	28128.5	325.18	34.58
RBF	(1,4)	1.91	669.2	3.56	0.41
	(1,5)	1.79	657.8	5.43	0.65
	(0.1,2)	2.19	816.0	7.13	0.60
	(0.1,3)	4.16	803.8	58.81	10.28
	(0.1,4)	1.07	215.6	6.89	1.06
	(0.1,5)	0.43	114.8	1.94	0.38
	(0.5,2)	4.42	1933.2	4.50	0.11
	(0.5,3)	5.34e4	1.88e7	3039.6	1632.0
	(0.5,4)	1.07	352.2	2.38	0.28
	(0.5,5)	1.75	466.6	4.78	0.66
	(1,2)	2.92e4	7.92e6	1720.8	1512.4
	(1,3)	3.61e6	1.27e9	8.09e4	8.00e4
	(1,4)	2.17	714.8	5.23	0.61
	(1,5)	3.62	969.4	10.97	1.44

TABLE 4: **Example 3:** Control-effort metrics. Total variation of the input (TV_u) and peak input magnitude ($Peak_u$). Higher TV_u indicates stronger actuation. The radial-basis-function (RBF) kernel yields the smoothest input, followed by the linear and unitary cases. The results show that the unitary kernel yields the largest overall actuation and highest peak input, matching its stronger overshoot seen in the output trajectories. The linear kernel exhibits slightly reduced total variation, while the RBF kernel provides the smoothest control action, giving the smallest TV_u and the lowest peak amplitude. These numerical values are consistent with the transient behavior in Figure 9, where the RBF response is fastest and least oscillatory.

Kernel	TV_u	$Peak_u$
RBF	2.359	0.277
Linear	3.810	0.320
Unitary	3.985	0.533

TABLE 5: **Example 4:** Performance metrics. Root-mean-square error (RMSE) and integral absolute error (IAE) quantify output tracking accuracy; total variation of the input (TV_u) and peak input magnitude ($Peak_u$) characterize input activity. Linear and polynomial kernels produce the lowest tracking errors and similar input activity, indicating nearly identical behavior. Unitary and radial-basis-function (RBF) kernels exhibit higher RMSE and IAE, along with increased input variation and larger control peaks. All methods remain stable and bounded, consistent with the parameter evolution shown in Figures 14 and 15.

Kernel	RMSE	IAE	TV_u	$Peak_u$
Linear	0.0817	5.75	5.26	0.71
Polynomial-2	0.0819	5.72	5.23	0.71
Unitary	0.121	30.29	7.05	0.83
RBF	0.134	28.94	9.09	0.90

TABLE 6: **Example 5:** Performance metrics. Root-mean-square error (RMSE) and integral absolute error (IAE) quantify output tracking accuracy; total variation of the input (TV_u) and peak input magnitude ($Peak_u$) characterize control activity. The polynomial kernel attains the smallest tracking error in both RMSE and IAE, reflecting its direct representation of the cubic cross terms. The linear kernel delivers intermediate accuracy, whereas the unitary and radial-basis-function (RBF) kernels show the largest residuals, consistent with their observable steady-state biases. All methods exhibit similar control activity, with TV_u and $Peak_u$ confined to a narrow range, indicating that the polynomial kernel's higher accuracy is not achieved through increased control effort. These findings support the conclusion that explicit polynomial features provide the most balanced performance in this nonlinear setting.

Kernel	RMSE	IAE	TV_u	$Peak_u$
Polynomial-2	0.1184	15.41	1.527	0.165
Linear	0.1277	23.31	1.536	0.164
Unitary	0.1586	34.01	1.560	0.184
RBF	0.1667	36.74	1.539	0.187

TABLE 7: **Example 6:** Performance metrics. Root-mean-square error (RMSE) and integral absolute error (IAE) quantify output tracking accuracy; total variation of the input (TV_u) and peak input magnitude ($Peak_u$) characterize control activity. The polynomial kernel achieves the smallest RMSE and IAE, consistent with its accurate representation of the cubic input nonlinearity. The linear kernel provides intermediate accuracy, whereas the unitary and RBF kernels produce larger tracking errors and greater accumulated deviations. Among these, the unitary kernel yields the highest IAE, matching its visible undershoot and slower convergence. Control activity measures, including TV_u and $Peak_u$, remain similar across all kernels, indicating that the polynomial kernel's improved accuracy does not rely on elevated input effort. These numerical outcomes reinforce the ranking implied by the plots.

Kernel	RMSE	IAE	TV_u	$Peak_u$
Polynomial-2	0.2546	109.93	3.00	0.458
Linear	0.2682	150.54	2.77	0.387
RBF	0.3188	290.09	1.77	0.271
Unitary	0.3909	436.27	2.37	0.295

TABLE 8: **Example 7:** Performance metrics for attitude stabilization. Lower values of root-mean-square error (RMSE) and integral absolute error (IAE) indicate higher tracking accuracy; total variation of the input (TV_u) and peak input magnitude ($Peak_u$) quantify control activity. Although the linear and polynomial kernels appear to converge more slowly in the time-domain plots (see Figure 22), their steady-state tracking accuracy, which is measured by RMSE and IAE, is superior. This follows from the fact that the performance metric includes the angular-velocity components of the output vector, and the linear and polynomial kernels produce smoother responses with reduced velocity amplitudes. As a result, their trajectories remain closer to the reference, which is zero for both attitude and angular rate, despite slower transient convergence. The unitary and radial-basis-function (RBF) kernels reach equilibrium more rapidly but with slightly larger velocity excursions, leading to higher accumulated error. Control activity is similar across all methods, indicating that the accuracy differences stem from the trade-off between transient speed and overall output smoothness rather than variations in control effort.

Kernel	RMSE	IAE	TV_u	$Peak_u$
Polynomial-2	0.1184	15.41	1.5269	0.1653
Linear	0.1277	23.31	1.5359	0.1641
Unitary	0.1586	34.01	1.5604	0.1842
RBF	0.1667	36.74	1.5394	0.1873

TABLE 9: **Example 6** (Appendix): Performance metrics under additive measurement noise stress. Root-mean-square error (RMSE) and integral absolute error (IAE) quantify output tracking accuracy; total variation of the input (TV_u) and peak input magnitude ($Peak_u$) characterize control activity. The ranking of the kernels remains consistent with the noiseless case: the polynomial kernel attains the lowest RMSE and IAE, followed by the linear kernel, while the unitary and radial-basis-function (RBF) kernels display larger tracking errors. The uniform increase in all error metrics reflects the influence of measurement noise, yet all trajectories stay bounded and stable. Control activity measures (TV_u , $Peak_u$) remain similar across kernels, indicating that the polynomial kernel preserves its accuracy without additional input effort. These numerical results align with the trends visible in Figure 24.

Kernel	RMSE	IAE	TV_u	$Peak_u$
Polynomial-2	0.2546	109.93	3.00	0.458
Linear	0.2682	150.54	2.77	0.387
RBF	0.3188	290.09	1.77	0.271
Unitary	0.3909	436.27	2.37	0.295

Author Biography

² **Tam W. Nguyen** received the M.Sc. degree in mechatronics engineering and the Ph.D. degree in control systems from the Free University of Brussels, Belgium. He then served as a postdoctoral
⁴ researcher in the Aerospace Engineering Department at the University of Michigan, Ann Arbor, US. Afterwards, he was appointed assistant professor at the University of Toyama, Japan, at the
⁶ Department of Electrical Engineering. He is currently a lecturer at the Kyoto University, Japan, in the Department of Electrical Engineering. His interests are in optimal control for aerial-robotic
⁸ applications.